GEORG-AUGUST-UNIVERSITÄT
GÖTTINGEN

Fakultät für
Physik

Master's Thesis

Entwicklung eines TCT-Messaufbaus für Sensormaterialien für Spurdetektoren in der Hochenergie-Physik

Development of a TCT Measurement Setup for Sensor Materials for Tracking Detectors in High-Energy Physics

prepared by

Christoph Klein

from Gießen

at the II. Physikalischen Institut

Thesis number:	II.Physik-UniGö-MSc-2014/09
Thesis period:	1st October 2013 until 30th September 2014
First referee:	Prof. Dr. Arnulf Quadt
Second referee:	Priv.Doz. Dr. Jörn Große-Knetter

Abstract

Im Hinblick auf den kommenden Upgrade des LHC werden verschiedene neuartige Sensormaterialien auf ihre Nutzung in Spurdetektoren untersucht. Zu diesem Zweck müssen die Materialien charakterisiert und ihre elektrischen wie auch optischen Eigenschaften bestimmt werden, insbesondere die Charge Collection Distance. Im Rahmen dieser Arbeit wurde daher ein Messaufbau für die Transient Current Technique entwickelt, mit welchem sowohl eine Siliziumdiode als auch ein pCVD-Diamant vermessen wurden.

Stichwörter: Hochenergiephysik, Halbleitersensoren, Diamant

Abstract

With regard to the upcoming upgrade of the LHC, several new sensor materials are investigated as to their use in tracking detectors. For this purpose, those materials have to be characterised in order to determine their electrical and optical properties, especially the charge collection distance. During the course of this thesis, a transient current technique measurement setup has been developed, with which a silicon diode as well as a pCVD diamond have been measured.

Keywords: high energy physics, semiconductor sensors, diamond

Contents

1 Introduction

Detectors for ionising particles and photons are commonly used in many research fields as well as today's technology. With respect to high-energy physics, detectors are employed to measure the energy, momentum, and trajectory of traversing particles, thus allowing an identification of events. Especially in the case of particle accelerators, the position of primary and secondary vertices is of utmost importance to determine the underlying physics of the decay. Therefore, the inner detector layers of the majority of current collider experiments, such as Atlas and Cms, consist of a pixel detector among others.

However, since pixel detectors form the innermost layers, they are located nearby the interaction point, hence sensor and electronics are exposed to large fluences of high-energy ionising particles. The result is increasing radiation damage, which subsequently yields a diminishing performance of the detector components. For this reason alternative and more radiation hard detector materials are investigated for upcoming upgrades of the existing as well as currently planned particle colliders.

One of the technologies considered for the HL-Lhc upgrade is an inner pixel layer consisting of diamond with three-dimensional structured electrodes. Since diamond offers a unique combination of advantageous electrical and mechanical properties in addition to an enhanced radiation hardness in comparison to silicon, research is underway to develop the conditions for future applications. With the improvements of diamond synthesis via chemical vapour deposition (CVD), one of the problems regarding diamond, the large scale fabrication at affordable cost, is no longer the dominant factor. However, to assess the properties and capabilities of detector devices based on diamond, the underlying material has to be characterised. A possible method for characterisation is the transient current technique which can be used to measure electrical properties, such as the carrier mobility or the lifetime, of a semiconductor or insulator.

The following thesis presents the physical and experimental principles with regard to the application of the transient current technique (TCT) to pCVD diamond samples and silicon diodes. At first the theoretical foundations of the interaction and consequently the detection of particles in a vertex detector is described in addition to the basic functionality of a semiconductor pixel detector. The subsequent chapter deals with the details

of the fabrication and graphitisation of diamond towards the use as sensor devices. The principles, setup and results of capacitance measurements of silicon diodes is shown afterwards. The following chapter covers the basics and specifications regarding the transient current technique and the development until the final setup used to obtain the results for a silicon diode as well as a diamond sample, which are shown in the last chapters.

2 Pixel detectors

The detection of particles and light is a fundamental aspect, not only in high-energy physics, but also with respect to many appliances in everyday life. The principles of particle detection with emphasis on vertex measurement and pixel detectors are presented in the following.

2.1 Detection of particles

2.1.1 Heavy ionising particles

Assuming the charged particle traversing the material is much heavier than electrons ($M \gg m_e$), the predominant energy loss happens via ionisation and excitations of the material, resulting in (quasi-)free charge carriers in the vicinity of the trajectory. To measure the induced charge, these charge carriers can be extracted by an external electric field or light from the de-excitation can be detected. The quantum mechanical process for relativistic particles was first described by Bethe and Bloch [1, 2], determining the average energy loss in the approximation $M^2 \gg m_e^2 + 2m_e E$ as follows:

$$-\left\langle \frac{\mathrm{d}E}{\mathrm{d}x} \right\rangle = Kz^2 \frac{Z}{A} \frac{1}{\beta^2} \left[\frac{1}{2} \ln \frac{2m_e c^2 \beta^2 \gamma^2 T_{max}}{I^2} - \beta^2 - \frac{\delta(\beta\gamma)}{2} \right] \tag{2.1}$$

with (values taken from [3]):

$\beta = v/c$	velocity of the traversing particle in units of the speed of light c;
$\gamma = \frac{1}{\sqrt{1-\beta^2}}$	Lorentz factor;
I	average ionisation energy of the material;
T_{max}	maximum kinetic energy which can be imparted to a free electron in a single collision;
z	charge of the particle in units of the elementary charge e;
Z, A	atomic number and atomic mass respectively;
m_e	$\simeq 511\,\mathrm{keV/c^2}$, electron mass;

K	$= 4\pi r_e^2 m_e c^2 N_A \simeq 0.307\,\mathrm{MeV\,cm^2/g}$;
r_e	$= \frac{e^2}{4\pi\varepsilon_0 m_e c^2}$, classical electron radius;
ε_0	permittivity of free space;

The average energy loss is usually normalised to the mass density ρ of the material, thus rendering the equation essentially independent of the material, since the ionisation energy only contributes logarithmically and the Z/A ratio is approximately $\frac{1}{2}$. The average energy loss for different $\beta\gamma$ is illustrated in Fig. 2.1 in the case of μ traversing copper.

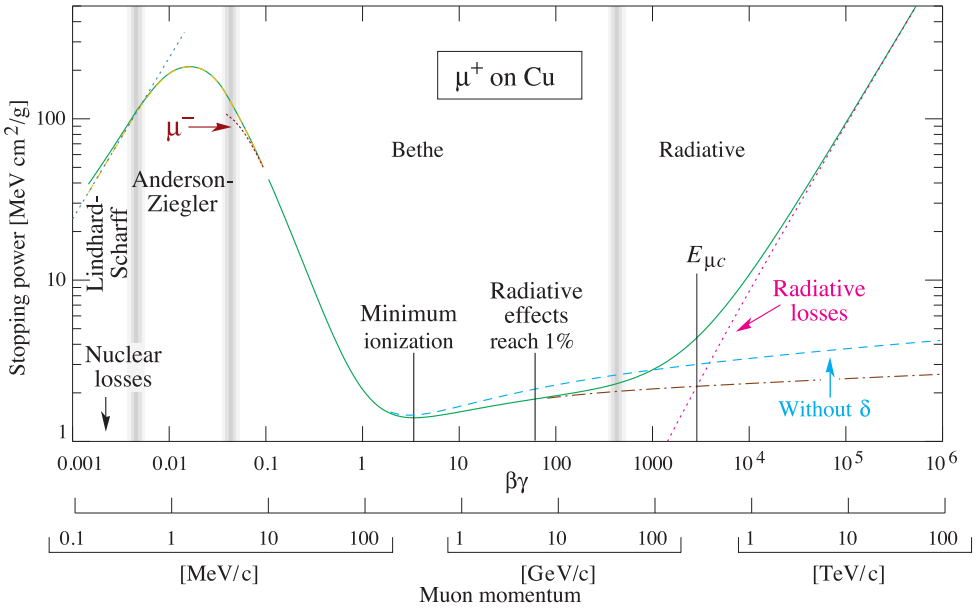

Figure 2.1: Energy loss of μ as a function of $\beta\gamma$ in copper absorber, illustrating the average energy loss according to Eq. 2.1. Boundaries between different approximations for several regions of kinetic energy are indicated by vertical lines [3].

Regarding the energy loss for small $\beta\gamma \lesssim 0.1$, the Bethe-Bloch formula is not yet valid, indicating other dominant processes in the interaction. For $\beta\gamma$ beyond the maximum, the $1/\beta^2$-term in Eq. 2.1 dominates, hence yielding a steep fall in the average energy loss resulting in a minimum at $\beta\gamma \approx 3\ldots4$ with $\langle \mathrm{d}E/\mathrm{d}x \rangle_{min} \approx 1.5\,\mathrm{MeV\,cm^2/g}$ nearly independently of the detector material. This minimum is often referred to as a hypothetical *minimum ionising particle* (m.i.p.), which is often used as the quantification of the detector response with no need for a specific particle. For higher $\beta\gamma$ the slow rise is proportional to $\ln(\beta\gamma)$, being further reduced for highly relativistic particles by the attenuation factor $\delta(\beta\gamma)$ in Eq. 2.1, such that the average loss only rises to values between 10 % to several 10 % above the minimum. The overall behaviour can be understood in a semi-classical approach derived in the book [4], with the $1/\beta^2$-term originating in the individual en-

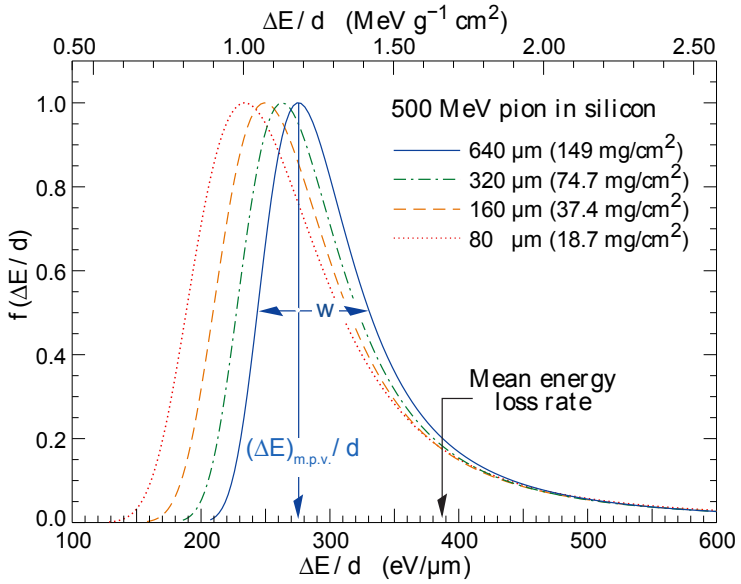

Figure 2.2: Landau distribution, described by Eq. 2.2, of the energy loss rate ΔE of a m.i.p. in silicon with varying thickness d and normalized to d. The average value, as obtained from the Bethe-Bloch formula, is independent of absorber thickness as indicated, only the most probable value changes [3].

ergy transfer of the scattering process, the logarithmic term coming from the Coulomb potential, and the attenuation being due to material dependent polarisation effects. In addition, with respect to μ traversing a material, as shown in Fig. 2.1 for kinetic energies in the TeV-region, radiative effects become dominant with regard to the energy loss by ionisation as described by the Bethe-Bloch formula. These processes are dependent on the particle mass and thus vary for different incident particles. A more detailed description of the energy loss of heavy charged particles can be found in the respective chapter of the "Review of Particle Physics", published by the Particle Data Group (PDG) [3].

Since energy loss is a statistical process and the Bethe-Bloch formula only describes the average value, the actual distribution of the total deposited energy has to be taken into account. Due to the fact that many of the individual scattering processes only lead to a small energy deposition with respect to the maximum possible kinetic energy transfer T_{max}, the total deposited energy ΔE is highly skewed for a small number of interactions, i.e. thin material. The probability distribution of energy deposition in thin absorbers is described by a *Landau-Vavilov distribution* [5, 6]

$$L(\lambda) = \frac{1}{\pi} \int_0^\infty \mathrm{e}^{-u \ln(u) - u\lambda} \sin(\pi u)\, \mathrm{d}u \tag{2.2}$$

with

$$\lambda = \frac{\Delta E - (\Delta E)_{\text{m.p.v.}}}{\xi} \qquad \text{and} \qquad \xi = \frac{K}{2} z^2 \frac{Z}{A} \frac{1}{\beta^2} \rho d \tag{2.3}$$

where d is the thickness of the material and

$$(\Delta E)_{\text{m.p.v.}} = \xi \left[\ln\left(\frac{2 m_e c^2 \beta^2 \gamma^2}{I} \right) + \ln\left(\frac{\xi}{I} \right) + j - \beta^2 - \delta(\beta\gamma) \right] \tag{2.4}$$

denotes the most probable value of the total energy deposition with $j = 0.2$ according to [7]. The Landau distribution for a m.i.p. traversing silicon with varying thickness is illustrated in Fig. 2.2. The asymmetric behaviour of the skewed distribution is apparent, whereas the average energy deposition $\langle \Delta E \rangle / d = \langle \mathrm{d}E/\mathrm{d}x \rangle$ remains constant, as described by the Bethe-Bloch formula Eq. 2.1. Moreover, it can be shown that while $\mathrm{d}E/\mathrm{d}x$ is independent of thickness, $(\Delta E)_{\text{m.p.v.}}/d$ scales $\propto \ln d$.

The transition from thin to thick material is defined by the parameter

$$\kappa = \frac{\xi}{T_{max}} \tag{2.5}$$

with $\kappa \to 0$ describing thin absorbers. $\kappa \to \infty$ indicates the case of thick absorbers, for which the distribution of the total deposited energy becomes Gaussian, due to the central limit theorem by interpreting thick absorbers as multiple thin layers. The transition case between thin and thick material has also been described in the work [6] by Vavilov.

2.1.2 Electrons and photons

In contrast to heavy ionising particles, for incident electrons the energy loss due to bremsstrahlung in the electric field of the nuclei of the absorber material, as described in [8], cannot be neglected, thus leading to several terms in addition to the Bethe-Bloch formula. However, the general behaviour in the valid energy region remains as already discussed. Since the energy loss of electrons because of bremsstrahlung is proportional to the energy E of the traversing particle and the proportionality constant only depends on material and particle properties, the process can be described by

$$-\left(\frac{\mathrm{d}E}{\mathrm{d}x} \right)_{rad.} \equiv \frac{E}{X_0} \tag{2.6}$$

The *radiation length* X_0 is a material property which combines the proportionality constants of energy loss via bremsstrahlung. It is the length after which the incident energy

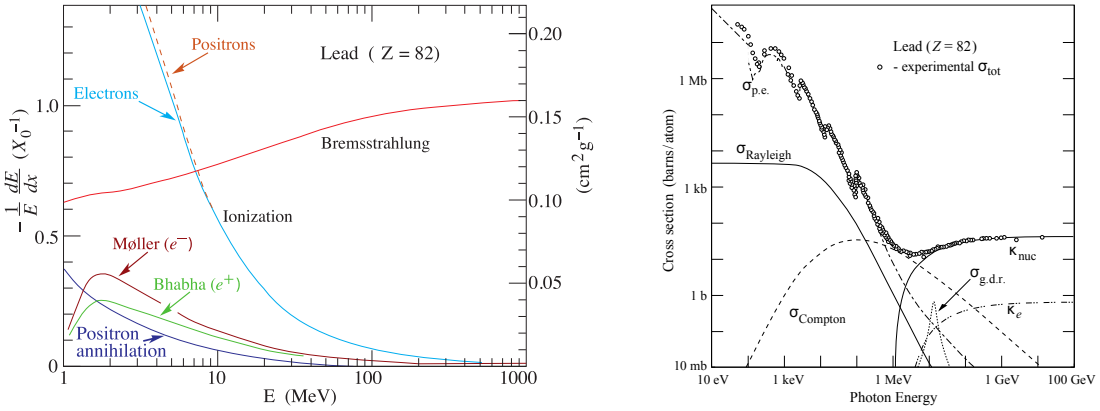

(a) (b)

Figure 2.3: (a) Fractional energy loss of $e^{\pm}$ per radiation length and (b) photon total cross section in lead as functions of incident energy, showing the contributions of different processes [3].

E_0 of an electron is reduced to E_0/e due to bremsstrahlung.

The interaction of photons with an absorber material is substantially different in comparison to charged particles. There are three dominating processes which can occur depending on the energy of the incident photon:

photo-absorption: For photon energies close to but larger than the binding energy of shell electrons in the material, the photon is completely absorbed by the electron which in turn becomes a free charge carrier with a kinetic energy equal to the difference of photon and binding energy.

Compton scattering: If the photon energy is well above the binding energy, the photons scatter off the shell electrons, which can be considered quasi-free, with a fraction of the photon energy transferred to the electron.

pair-creation: Photons with an energy exceeding twice the electron mass can create electron-positron pairs in the absorber.

In the case of high-energy physics, only pair-creation has to be taken into account for the components of tracking and vertex detectors. Pair-creation is an overall unwanted process for these devices, because of the additional tracks increasing the occupancy in the tracking detector, which is especially problematic in the case of a hadron collider with an already highly occupied detector. Moreover, measurements of the photon properties may be altered, since it is more difficult to reconstruct the properties from the additional tracks. Due to the similarities between the processes of bremsstrahlung and pair-creation,

the *mean free path* λ of photons also depends on the radiation length of the material:

$$\lambda = \frac{9}{7} X_0 \tag{2.7}$$

As a consequence, tracking detectors are required to have small X_0 to provide low pair-creation probability and hence to ensure the overall stability and efficiency of the whole detector.

2.2 Vertex measurement

The development of pixel detectors for applications in particle physics has been mainly motivated by two important requirements: The ability to study short lived particles decaying into secondary ones and the capability to cope with the increasing number of interaction rates and energies. For the first requirement particle tracks have to be measured and extrapolated to determine whether their common origin is a decay vertex which differs significantly from the interaction point. The latter point requires the detector to be able to detect multiple tracks and select the hit patterns of interest. As consequence, sufficiently high spatial resolution is needed, which is primarily determined by the *pitch*.

The spatial resolution of a pixel with pitch p can be calculated in the exemplary case of a pixel with a single threshold binary readout centred around the position 0. In this case one assumes only one pixel per track to be triggered in addition to a uniform density of incident particles. The resulting one-dimensional spatial resolution is

$$\sigma_x = \sqrt{\mathrm{Var}(\Delta x)} = \sqrt{\frac{1}{p} \int_{-p/2}^{p/2} x^2 \, \mathrm{d}x} = \frac{p}{\sqrt{12}} \tag{2.8}$$

That means that the actual impact position of an incident particle differs from the measured position by $p/\sqrt{12}$ on average [9]. However, this value can be further improved if a group of pixels, a so called *cluster*, is triggered due to *charge sharing* between neighbouring electrodes. Hence using the optimal configuration for pixels in order to allow charge sharing essentially halves the pixel pitch.

The principles of vertex reconstruction can be derived in a simple detector model consisting of two segmented layers located around the beam axis at radii r_1 and r_2 with $r_1 < r_2$, respectively, and a one-dimensional spatial resolution of σ_1 and σ_2. The *impact parameter*, i.e. the distance to the interaction point, of the vertex position d_0 can be determined by measuring the hits in the individual layers and extrapolating the track to

$r = 0$ up to a resolution of

$$\sigma_{d_0}^2 = \frac{r_2^2\sigma_1^2 + r_1^2\sigma_2^2}{(r_2 - r_1)^2} \tag{2.9}$$

Apart from the limited precision due to the segmentation, there are additional contributions from multiple scattering in the beam pipe wall, resulting in a distribution and hence a smearing of the particle direction:

$$\sigma_\theta \approx \frac{13.6\,\text{MeV}}{pv}\sqrt{\frac{d}{X_0}} \tag{2.10}$$

with the momentum p and velocity v of the particle traversing a material with thickness d and radiation length X_0. Thus the net uncertainty yields a constant term depending on the geometry and the term for multiple scattering depending on material and decreasing with p.

With respect to the vertex resolution, there are several ways to improve the tracker design. Eq. 2.9 suggests the inner radius to be as small as possible, moreover, the outer radius should be as large as possible. On the other hand, these suggestions are limited either by the beam pipe, the track density near the interaction point, and the radiation damage for the inner radius, or the costs for large tracking detectors in the case of the outer radius. The contribution of multiple scattering is negligible for large particle momenta. However, thin detectors and a large radiation length are important.

Vertex detectors are usually located inside an intense magnetic field B, leading to a deflection of the trajectories of charged particles due to the Lorentz force. The resulting curvature of incident particle tracks can be used to determine the particle momentum, provided at least 3 layers of tracking devices are triggered. Thus the complete trajectory of a particle can be measured. Apart from incident particles, charge carriers within the detector are also deflected by the *Lorentz angle* θ_L [9]:

$$\tan\theta_L = \mu_H B \approx \mu B_\perp \tag{2.11}$$

where $B_\perp$ is the magnetic field component perpendicular to the electric field within the detector, μ_H the *Hall mobility* and μ the respective carrier mobility (see Section 5.1).

2.3 Hybrid pixel detectors

The general idea of hybrid pixel detectors is the separation of sensor and readout chips in the detector, illustrated in Fig. 2.4(a). The signal is generated in a sensor chip, which in the case of the pixel detectors of the LHC experiments have a thickness of $\sim 200-300\,\mu$m, the amplification and signal processing is done in a dedicated front-end readout chip, which includes the necessary electronics and is connected to the sensor, e.g. via bump bonds. Thus there is a 1:1 correspondence between pixels in the sensor and the readout chip, as shown in Fig. 2.4(b).

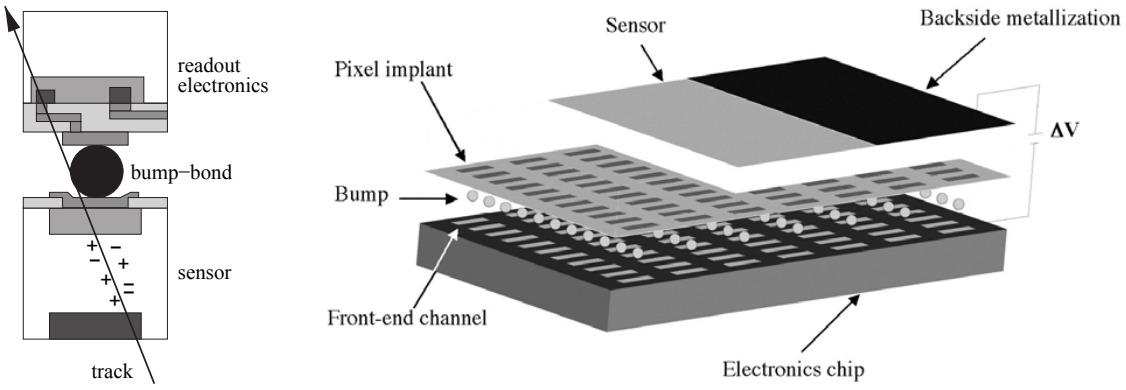

Figure 2.4: (a) Schematic view of a single pixel with an ionising particle traversing the detector and creating a signal charge, which is amplified and processed in the readout chip; (b) Sketch of a "blown-up" hybrid pixel detector [9].

Apparent advantages of such a detector setup are the separately produced, hence independently optimised, sensor and readout chips. Among others, even different underlying materials are possible. In general, hybrid pixels provide a very fast and parallel readout with subsequent processing, a decent inherent radiation hardness (additional aspects of radiation damage in Section 2.4) and a relatively large signal in comparison to other detector concepts. Furthermore, the overall mature technologies of semiconductor p-n junctions and CMOS lead to affordable cost with respect to the total detector area. However, the interconnection between sensor and electronic chip, often achieved via bump bonds, is not only a challenging technology but also rather costly. Moreover, the material budget, including the two chips as well as the necessary cooling and support structures, increases the probability of unwanted processes such as pair creation and multiple scattering in the vertex detector. Apart from these aspects, the pixel size is limited due to the direct coupling to the size of the electronics cell.

In the following, the principles of hybrid pixel detectors are presented with respect to the most commonly used sensor material: silicon.

2.3.1 Silicon sensors

Generated charge carriers in a semiconductor can be detected if the sensor is depleted of intrinsic free charge carriers and a sufficient external electric field is applied which separates the charge carriers. Already during the drift to the readout electrodes, a signal is induced which can be measured (see Section 5.1). The conceptual idea to achieve this is the usage of a p-n junction with applied reverse bias in the sensor material.

p-n junction

The number of free charge carriers in a semiconductor as well as their temperature dependency can be altered significantly by implementing *acceptor* or *donor* atoms as dopant in the crystal. Acceptors or donors, which replace silicon in the lattice, create a *p-* or *n-type* material with localized energy levels close to the valence or conduction band edge, respectively. Hence for the transition to the conduction or valence band only energies comparable to $k_B T$ at room temperature are needed, providing additional electrons (n-type) or holes (p-type) as free charge carriers. The remaining donor atoms become positive *space charges* and accordingly acceptors become negative ones. The following aspects and equations describing a p-n junction are presented according to the work [10].

A p-n junction, as illustrated in Fig. 2.5, is created between p-type, with holes as majority charge carriers, and n-type material, with electrons as majority carriers. The concentration difference of the majority carriers yields a diffusion of respective carriers at the junction. The electric field caused by these space charges subsequently compensates the diffusion leaving the vicinity of the p-n junction fully depleted of free charge carriers, thus resulting in a *space charge region* (SCR), also called *depletion zone*. The properties of the electric field can be derived from the Poisson equation

$$-\frac{\mathrm{d}^2 v}{\mathrm{d}x^2} = \frac{\rho(x)}{\varepsilon_{\mathrm{Si}}\varepsilon_0} \qquad \text{with} \qquad \rho(x) = \begin{cases} eN_D & \text{for} \quad 0 < x < x_n \\ -eN_A & \text{for} \quad -x_p < x < 0 \end{cases} \tag{2.12}$$

which leads to the electric field described by

$$E(x) = \begin{cases} \frac{eN_D}{\varepsilon_{\mathrm{Si}}\varepsilon_0}\,(x - x_n) & \text{for} \quad 0 < x < x_n \\ -\frac{eN_A}{\varepsilon_{\mathrm{Si}}\varepsilon_0}\,(x + x_p) & \text{for} \quad -x_p < x < 0 \end{cases} \tag{2.13}$$

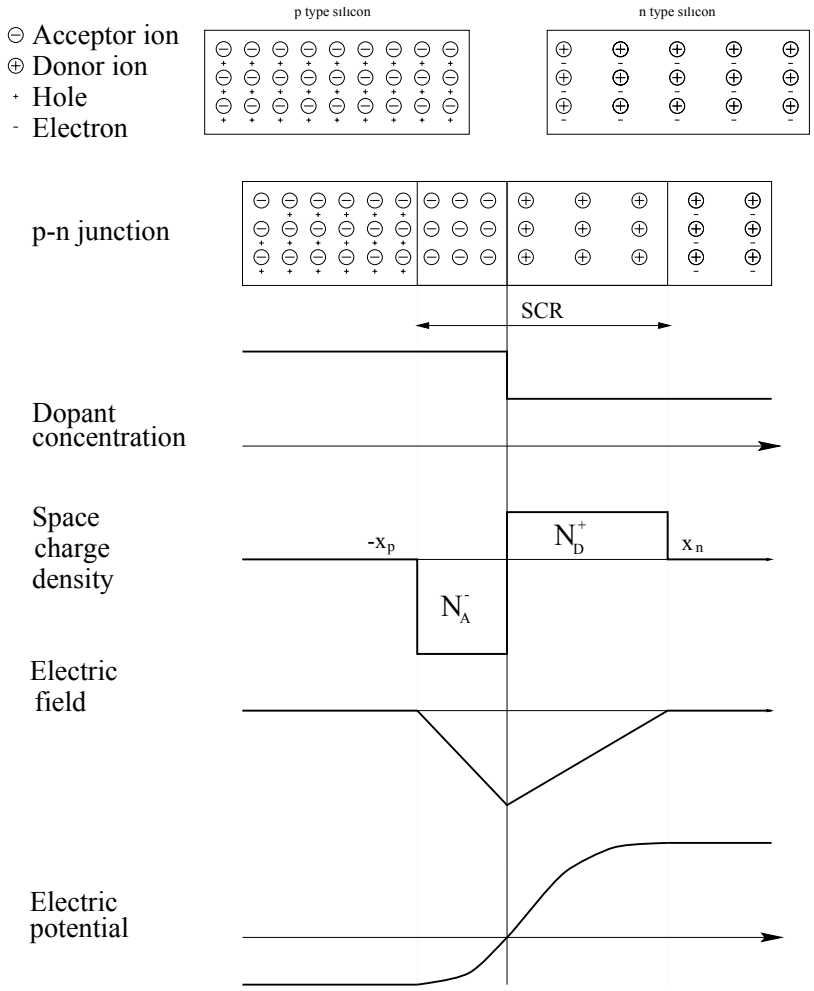

Figure 2.5: p-n junction in position space: dopant concentration, space charge density, electric field strength and electric potential [10].

with the extension of the depletion zone in the p- and n-doped material x_p and x_n respectively, as well as $\varepsilon_{\mathrm{Si}} = 11.75$ being the dielectric constant for silicon and ε_0 denoting the electric field constant. The continuity of the electric field provides neutrality of the entire silicon detector with $N_D x_n = N_A x_p$. Moreover, since the used p-n junctions usually contain one thin but highly doped implant and a lightly doped bulk, one can assume $N_A \gg N_D$ and $x_n \gg x_p$ in the case of p-pixel in n-type silicon or vice versa $N_A \ll N_D$ and $x_n \ll x_p$ for n-in-p. Thus the depletion depth d is approximately equal to the extension in the lightly doped material. Considering the fact that semiconductors usually contain both donors and acceptors due to impurities results in an effective doping concentration $N_{\mathrm{eff}} = N_D - N_A$.

The electric field corresponds to a built-in potential within the material

$$U_{\mathrm{bi}} = \int_{-x_p}^{x_n} E(x)\,\mathrm{d}x = \frac{e}{2\varepsilon_{\mathrm{Si}}\varepsilon_0}\left(N_D x_n^2 + N_A x_p^2\right) \approx \frac{e\,|N_{\mathrm{eff}}|\,d^2}{2\varepsilon_{\mathrm{Si}}\varepsilon_0} \tag{2.14}$$

An external voltage will either increase the depth of the depletion zone if applied in the same direction as U_{bi} (*reverse bias*) or reduce it (*forward bias*). The depletion depth d is hence calculated with respect to Eq. 2.14 as follows:

$$d \approx \sqrt{\frac{2\varepsilon_{\mathrm{Si}}\varepsilon_0\,(U_{\mathrm{ext}} - U_{\mathrm{bi}})}{e\,|N_{\mathrm{eff}}|}} \tag{2.15}$$

The permanent thermal generation of charge carriers and subsequent separation in the depletion zone leads to a *leakage current* throughout the sensor volume

$$I_{\mathrm{Vol}} = \frac{en_iAd}{2\tau} \;\propto\; T^{\frac{3}{2}} \cdot \exp\left(-\frac{E_g}{2k_BT}\right) \tag{2.16}$$

with n_i being the intrinsic charge carrier density, A the area of the junction, d the depletion depth, and τ the lifetime of the minority carriers. Other effects such as surface currents as well as charge carrier generation in defects and damaged parts of the crystal contribute to the overall leakage current of the sensor.

Contacting and biasing of detectors

Due to the difference of the Fermi and vacuum levels in metals and semiconductors, a metal-semiconductor contact usually results in a *Schottky contact* including a potential barrier that prevents efficient charge carrier transport into the semiconductor. The solution to this issue is the usage of highly doped layers for the contact. Because of the doping the difference in Fermi levels becomes smaller, thus yielding a small junction between metal and semiconductor through which charge carriers can tunnel. Hence the junction behaves like an ohmic contact. Since the pixel layer is already highly doped only the opposite side of the sensor is provided with an additional highly doped thin layer of the same type as the bulk spanning the whole surface of the sensor chip.

The biasing of the sensor can be done by various techniques. The most straightforward would be a resistor network, which can be implemented using polysilicon structures. However, one can also exploit the lateral growth of a depletion zone to bias a p-n junction without directly contacting it. This *punch-through* mechanism happens if an external voltage is applied to another p-n junction in the vicinity of the readout contact such that

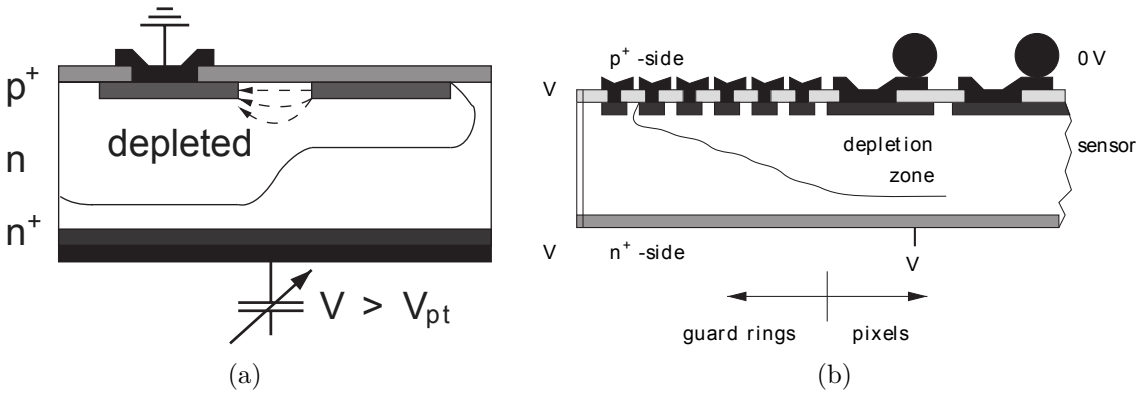

Figure 2.6: (a) Punch-through effect illustrated with the depletion zone of the biasing contact reaching the intrinsic zone of the active sensor; (b) Depletion region below guard rings and potential of surfaces and edges [9].

the depletion zone of the biased contact reaches the intrinsic zone of the readout contact. The effect is shown in Fig. 2.6(a). The voltage at which the depletion zone extends to the readout electrode is the punch-through voltage U_{PT}, hence the depletion zone in the active sensor grows with increasing bias voltage U_{ext} together with the depletion zone of the biasing contact. The resulting reverse bias at the readout electrode is therefore the difference $U_{\text{ext}} - U_{PT}$, with the exact quantity U_{PT} depending on the distance between the two junctions, the concentration of the dopant and the potential distribution in the sensor bulk.

The punch-through mechanism is also used to avoid leakage current at the sensor edge. The bias voltage is usually applied on the back plane, whereas the pixel implants are grounded by the electronics. The main problem arising is that mechanical damage at the cutting edges of the silicon wafers cannot be completely avoided thus being conductive. Due to this effect the potential of the surface between the cutting edge and the active area will be between the ground potential and the bias voltage and in the extreme case equal to either one. If the potential at the cutting edge is approximately equal to the ground potential, the depletion zone reaches the surface, hence the surface defects inject a large leakage current into the active area. If the surface is at the bias potential, accumulated charge carriers form a conductive layer close to the pixel implant yielding a high local electric field and leading to the risk of a sensor breakdown. Implementing *guard ring* structures, floating highly doped rings of the same type as the pixels as shown in Fig. 2.6(b), around the active area leads to a potential drop between each subsequent ring through the punch-through mechanism until the outermost ring reaches the bias potential thus preventing the depletion zone from reaching the cutting edge.

2.3.2 Detector readout

The following section contains a brief summary of general aspects regarding readout electronics. The basics of charge carrier transport and induced signals are described in the later Sections 5.1 and 5.1.1.

Even though many different pixel geometries, readout techniques, and analogue circuits exist for pixel detectors, with respect to the intended use, many parts of a general design are common among most of them. In general, the chips are divided into an *active area* for each corresponding pixel, with sensitivity to incident particles or photons, respectively, and the *chip periphery* containing the controlling elements and data buffering. A typical front-end circuit is shown in Fig. 2.7.

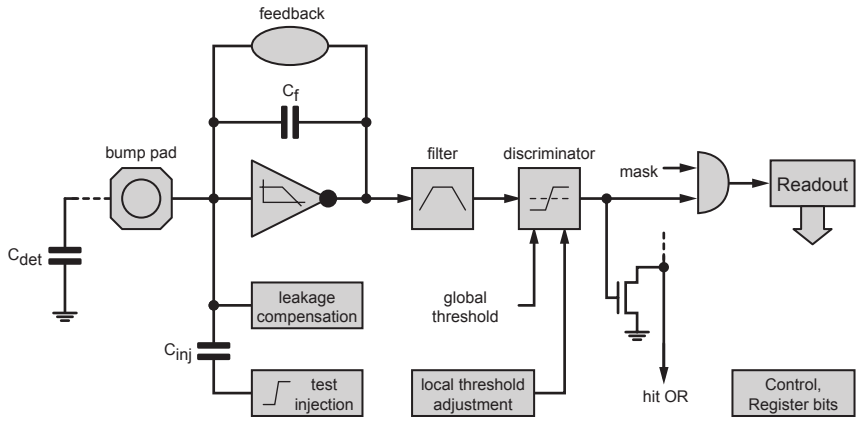

Figure 2.7: Schematic circuit of a typical front end cell. The sensor is represented by the capacitor C_{det} [9].

The generated charge of a signal is measured with an amplifier, the most common being a *charge-sensitive amplifier* (QSA), i.e. a device to directly measure the collected charge by integrating the current of a feedback capacitor C_f. A feedback circuit is required to define the DC operation point of the QSA as well as remove signal charges from C_f after the dynamic response of the amplifier. The choice of the applied feedback current is also critical for the measured signal, since either a too small feedback cannot discharge the capacitor in time with regard to the bunch crossing time, or a too large current reduces the signal even during the respective readout, hence leading to a *ballistic deficit*.

To modify the overall shape of the signal pulse and remove unwanted oscillations, a *CR-RC-shaper* is used, which is a differentiator and subsequent integrator acting as a high-pass and low-pass filter, respectively. After the shaping of the signal, the signal threshold is defined by a discriminator and hence it is decided whether the signal will be further processed. A common discrimination value is the *time over threshold* (ToT) of the signal.

2.4 Radiation damage

In particle physics, silicon sensors as well as the readout electronics suffer from radiation damage during operation due to the interactions of high-energy particles, which are produced in the particle collisions within the collider, with the nuclei of the material the detector components consist of. This aspect becomes an increasingly important issue as the development of particle accelerator experiments moves on to higher luminosities and hence radiation doses in the inner detector layers. Radiation induced defects can be divided into two categories, *surface* and *bulk damage*. Surface defects are especially important for the oxide structures of readout electronics, manifesting itself in charge accumulation and subsequent electrical breakdown. Regarding the sensor material, bulk damage, i.e. damage in the crystal lattice, is the dominating effect leading to diminishing performance over time, therefore it will be the main focus of this section.

Bulk damage originates from the interaction of incident particles which transfer sufficient energy to remove atom from the lattice. The necessary energy is called *displacement energy* and accounts for $\sim 20\,\mathrm{eV/atom}$ in silicon [11]. The underlying energy transfer is mediated by Coulomb interaction, as described by the Bethe-Bloch formula Eq. 2.1, for charged particles as well as nuclear forces in the case of neutrons. Lattice atoms removed from primary interactions can further remove additional secondary atoms, provided the residual kinetic energies of primary atoms still exceeds the displacement energy.

The displacement of single atoms may lead to empty lattice sites, so called *vacancies*, with the displaced atoms being repositioned between actual lattice sites, referred to as *interstitials*. These defects can occur in a local concentration within the material, hence bulk damage is further classified into *point* and *cluster defects*. Moreover, since thermal energy at room temperature provides mobility of the defects within the crystal, defects are generally unstable, thus they may *anneal* over time or arrange to more stable defect combinations. Further information about radiation hardness can be found in [12], annealing of defects is discussed in [13] and a general overview is given in the respective sections of the book [9].

The overall results of bulk damage are additional energy levels within the band gap. Defect levels which are located in the middle of the band gap usually act as recombination and generation centres because of the almost similar distance to the edges of the valence and conduction band, leading to a reduced charge carrier lifetime and measured charge. As opposed to these, defect levels in the vicinity of the band edges act as *trapping* centres of free charge carriers from the respective bands. Trapped charges are subsequently released with a delay in the order of μs. The result is, on the one hand, a modification of the

effective doping, i.e. space charge, concentration because of the overall removal of free charge carriers from the material and, on the other hand, a reduction of the net signal due to the delayed release of trapped charges.

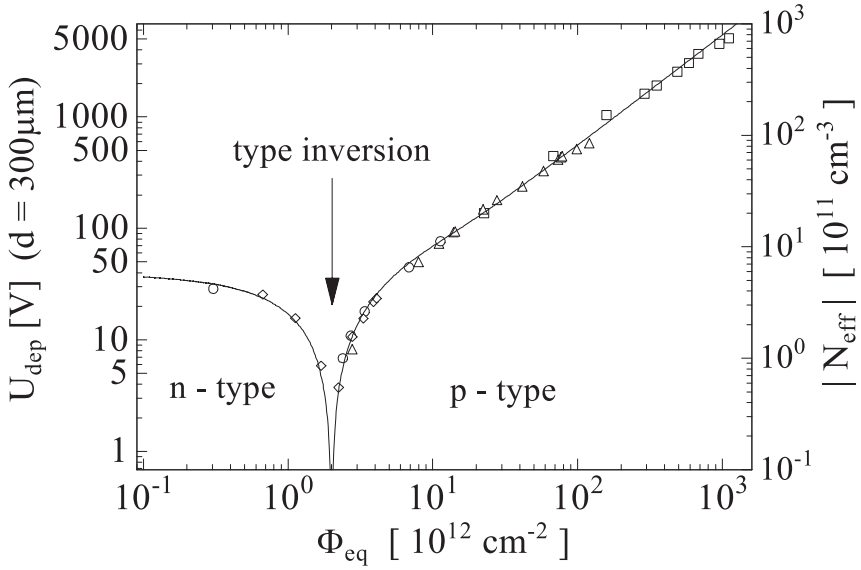

Figure 2.8: Change of the absolute effective doping and hence the full depletion voltage of a 300 μm thick silicon sensor versus the fluence normalized to 1 MeV neutrons [12].

The modification of the effective doping concentration has an even more severe consequence for the detector material. Since the depletion depth is dependent on the effective space charge concentration (see Eq. 2.15), a smaller N_{eff} subsequently reduces the depletion depth and accordingly increases the necessary voltage for full depletion, as shown in Fig. 2.8. Furthermore, for an original n-type bulk material, a modification in the effective doping leads to a change from n- to an effective p-type material in the case of high radiation doses, easily achievable with hadron colliders such as LHC, because of the generation of additional acceptor atoms due to radiative defects. Hence, because of this *type inversion*, the depletion zone not only grows in the opposite direction but this effect may yield an electric breakdown of p-in-n detectors. Therefore n-in-n pixels were used for the ATLAS and CMS pixel detectors. More importantly, radiation hard detector materials and concepts are investigated for upcoming upgrades as well as new accelerators. One of the most promising techniques uses diamond as a sensor material, which is further discussed in the following section.

3 Diamond sensors

Diamond as a substance provides extreme physical and chemical properties hardly matched by any other natural material, such as the highest thermal conductivity and stiffness, as well as extreme mechanical rigidity and good radiation hardness. Moreover, it is optically transparent almost continually from the ultraviolet (UV) to the terahertz (THz) range and chemically inert. However, despite the potential as an engineering material, until the 1990s technological applications were limited due to the crystal size and the lack of the availability of consistent, high-purity material. With the first commercial products based on synthetic *chemical vapour deposition* (CVD) diamonds [14] and regarding today's rapid improvements in diamond synthesis, considerable research efforts are underway for their usage in a wide range of detectors.

This section describes the properties of diamonds which are important for detector application and remarks recent developments with respect to 3D diamond sensors.

3.1 Diamond: synthesis and properties

A wide range of detector applications and detector types make diverse demands on the material. In particle physics, diamond is already used in beam condition monitoring. Moreover, the usage as pixel detectors in tracking devices for future hadron colliders and the upcoming high-luminosity LHC upgrade is suggested. Other possible applications are, among others, neutron detection – e.g. in nuclear industry, dosimetry as well as fission and fusion research – or UV detection in harsh environment.

Natural diamond detectors, with detector material made from highly selected stones, might be used in several applications, however, they suffer from various issues regarding cost and availability. Only a small percentage of all naturally occurring diamonds are Type IIa – the most pure form, in contrast to Type Ia/Ib and Type IIb, without substantial nitrogen and/or boron impurities respectively – and, furthermore, only a small fraction of these might become useful detectors. Besides, even with extreme selection, the performance varies from one diamond to another and the typically very high material cost prevents the usage of natural diamond for large-scale detectors. Therefore only diamond

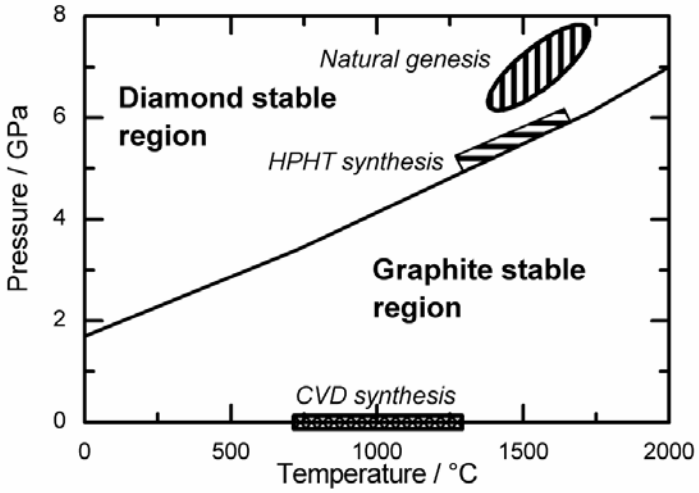

Figure 3.1: Phase diagram of carbon, the regions for stable diamond and graphite growth are shown as well as the pressure-temperature zones for metastable CVD synthesis, HPHT synthesis, and natural genesis are indicated [14].

synthesised by CVD is usable as they provide the required quality and have reduced cost.

3.1.1 Chemical vapour deposition of diamond

While the natural growth of diamond takes place at very high pressures and temperatures, about several GPa and $\gtrsim 1500°C$, in the chemical vapour deposition, diamond is grown in a non-equilibrium process. During the synthesis in CVD, carbon is deposited as graphite or diamond on a heated substrate. The required carbon is provided by the decomposition of a gaseous *precursor* containing carbon, e.g. hydrocarbon gases, at substrate temperatures ranging from about 700°C to 1200°C. In general, graphite grows much faster than diamond lattice, since it is the thermodynamically stable allotrope of carbon (as shown in Fig. 3.1) under these conditions. However, diamond growth is possible based on the kinetics of the growth surface and by using atomic hydrogen.

The presence of atomic hydrogen during the synthesis is of utmost importance for the deposition of diamond to be preferred over graphite in a metastable process. Atomic hydrogen terminates the surface of existing graphite or diamond structures on the substrate, yielding stable surfaces and preventing sp^2-type surface reconstruction. Additionally, it is used for etching away graphite from the surface due to its sp^2-bonds, hence leaving the comparatively inert diamond. The other critical reactions occurring in the gas-phase and during growth are similarly facilitated. The process itself can be separated into two steps: *nucleation* and *growth*. Nucleation starts with the adsorption of carbon on the substrate, which can be enhanced by providing nucleation centres in the form of lattice defects or

impurities and conditions to prevent subsequent immediate desorption.

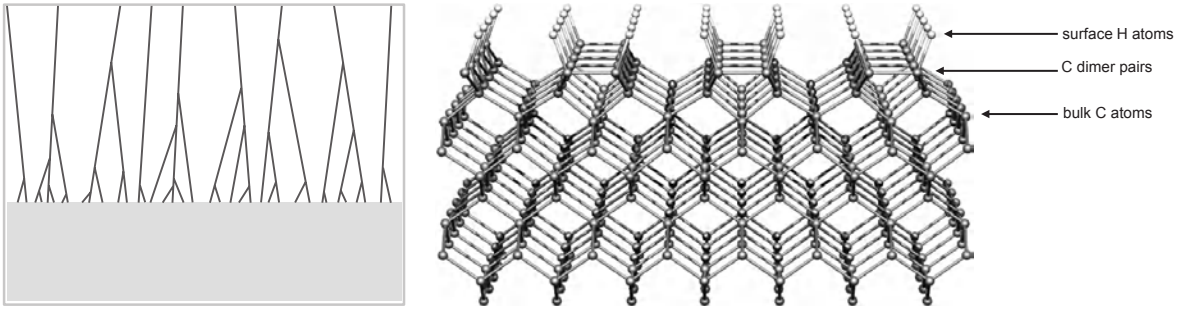

(a) (b)

Figure 3.2: (a) Illustration of a columnar grain growth in pCVD diamond with increasing grain size towards the growth side (up); (b) Single-crystal diamond viewed along a <110> direction with hydrogenated, hence terminated, surface in the {100} growth direction [15, chap. 2].

Diamond synthesised by CVD is *polycrystalline* (pCVD) by nature with a columnar structure of grains from the substrate to the surface. Typically, the columns increase and coalesce from the substrate to the growth side according to the van der Drift model of competitive grain growth [16], thus reducing the number of grain boundaries for later grown diamond due to inter-grown grains, as illustrated in Fig. 3.2(a). *Single-crystal* (scCVD) diamond of usable size can be produced by homoepitaxial growth in a microwave plasma assisted CVD reactor using {100} oriented single-crystal diamond substrate. In this case, high flux of atomic hydrogen during the growth leads to a hydrogenated diamond surface, as shown in Fig. 3.2(b). Regarding polycrystalline material, careful choice of nucleation and growth conditions leads to overall large and well-oriented grains as well.

3.1.2 Optical and electrical properties of diamond

Diamond crystals are formed of carbon atoms in a *diamond lattice* structure consisting of two face centred cubic (fcc) lattices displaced by one quarter of the diagonal length along the diagonal of the unit cell. Thus diamond comprises the lowest mass element which forms a stable covalently bonded crystal lattice. Moreover, the lattice is highly symmetric and tightly bound.

As it has been noted before, different types of CVD diamonds with differing properties can be produced and the material has to be selected for the respective use based on desired detector performance and requirements, e.g. detector area, decay time, operating voltage, and opacity. Most commercial CVD diamond technologies developed during the 1990s were based on pCVD diamond [17], which has the advantage of being grown in large areas,

albeit with many grains reducing the electronic performance. On the contrary, single crystal CVD diamond provides a high purity electronic grade without any grains, though the area size is limited due to the synthesis. After synthesis either type is polished to smooth the surfaces and take away low-quality material on the substrate side. Especially in the case of pCVD, this step provides an effective reduction of the number of grains if only the material from the growth side is left for further applications.

The main challenge of diamond detectors occurs from charge trapping. Especially the grain boundaries in pCVD diamond are an origin of traps which reduce the net signal of injected charges. Since traps provide a stable state for charges in the material, they can be filled by continuous *pumping*, i.e. keeping the traps occupied with additional charge carriers, thus reducing the effective number of charge traps. De-pumping of traps is possible by UV light. In contrast to pCVD diamonds, scCVD diamonds do not suffer from trapping due to the high crystal quality and consequent electrical purity.

A common figure of merit for the characterisation of CVD diamond detectors is the mean distance by which generated electron-hole pairs drift apart in an external electric field E before they are being trapped, the *charge collection distance* (CCD):

$$\mathrm{CCD} = (\mu_e \tau_e + \mu_h \tau_h)\, E \tag{3.1}$$

with $\mu_{e,h}$ and $\tau_{e,h}$ denoting the mobility and trapping time of electrons and holes as the respective charge carriers (see Section 5.1). Under the assumption that the detector thickness d exceeds the CCD ($d \gg \mathrm{CCD}$) and the electric field is uniform, the CCD can be measured by the ratio between induced and total deposited charge:

$$\mathrm{CCD} = d \cdot \frac{Q_{\mathrm{ind}}}{Q_0} \tag{3.2}$$

The general difference in the electric properties of single-crystal and polycrystalline diamonds arise in the respective charge carrier mobility as well as the CCD. While the electron as well as the hole mobility is large for either of the types, although depending on the crystal quality and thus higher for single-crystal material, the CCD accounts for the substantial difference. In the case of pCVD as pad detectors, the CCD is limited to $\sim 300\,\mu$m at $1\,\mathrm{V}/\mu$m electric field strength due to the impurities and grain boundaries responsible for charge trapping in the crystal [11]. On the contrary, the CCD of scCVD diamonds is only limited by the material thickness itself because of the absence of trapping.

In addition, diamond has the highest room temperature thermal conductivity of any material. The value is about the fivefold of copper and typically orders of magnitude larger

than that of any other optical material. This leads to reduced temperature gradients in the diamond itself as well as in any other component bonded to the diamond. Furthermore, the high thermal conductivity makes diamond an interesting material for application where active cooling of the detector components is either impractical or impossible [11].

Other relevant properties are discussed in the following in comparison to the respective properties of silicon, indicating advantages and disadvantages over the well-known and established material.

Comparison between diamond and silicon

While silicon is an established detector material for scientific and electronic applications with a well-developed industry, it suffers from radiation damage in high-radiation environment among others, reducing the overall reliability with regard to long-term operation. Considering this fact, diamond has the advantage of a more tightly bound crystal lattice, though of the same structure type, resulting in a more than twofold displacement energy. Moreover, since diamond is an insulator with a high resistivity by nature, in contrast to silicon, it does not require the depletion of intrinsic charge carriers and a reverse bias to work as a sensor. For this reason, diamond does not suffer from reduced depletion zones or type inversion for higher fluence, unlike silicon.

Given that the band gap of diamond is much larger, diamond detectors can be consequently operated with a very low leakage current, even in high-radiation environments. In addition, the low leakage current, hence low power dissipation, in conjunction with the already discussed high thermal conductivity supports the operation of diamond detectors with diminished power consumption. The lower dielectric constant leads to a reduced capacitive load on the detector front-end electronics, thus improving the noise performance. The overall high carrier mobility, regardless if electrons or holes, and the high saturation velocity in combination with a high breakdown voltage enables fast signal response and readout.

However, the large band gap also diminishes the primary charge generation due to incident particles. Moreover, charge trapping, especially in the case of pCVD diamond sensors, further reduces the measured charge and the resulting signal current. Additional notable properties of silicon and diamond are compared in Tab. 3.1.

3.2 3D diamond sensors

Considering the problem of the low CCD of polycrystalline CVD diamonds, a possible solution is the usage of 3D electrodes. This technology has already been investigated with

property		diamond	Si
band gap	[eV]	5.47	1.12
breakdown field	[V/cm]	10^7	3×10^5
resistivity	[Ω cm]	$> 10^{15}$	2.3×10^5
intrinsic carrier density	[cm^{-3}]	$< 10^3$	1.5×10^5
electron mobility	[$\mathrm{cm}^2\,\mathrm{V}^{-1}\,\mathrm{s}^{-1}$]	1500 . . . 2400	1450
hole mobility	[$\mathrm{cm}^2\,\mathrm{V}^{-1}\,\mathrm{s}^{-1}$]	1000 . . . 2100	≈ 440
dielectric constant		5.7	11.9
displacement energy	[eV/atom]	43	13-20
energy to create eh pair	[eV]	13	3.6
radiation length	[cm]	12.2	9.4
avg. signal created/μm	[e]	36	89
avg. signal created/0.1 % rad. length X_0	[e]	4400	8400

Table 3.1: Properties of diamond and silicon [11, 18].

respect to the improvement of silicon detectors. However, the proposed method to create these electrodes in diamond differs greatly from silicon, namely the conversion of diamond material to graphite, the so called *graphitisation*, is used to fabricate conducting channels in the sensor.

The basic principles and advantages of 3D electrodes are described in the following section, the subsequent one focuses on the graphitisation of diamond lattice.

3.2.1 Principles of 3D detectors

The main idea of 3D electrodes, as the name suggests, is the processing of electrodes nearly through the entire detector bulk material. Contrary to sensors fabricated with planar electrodes on the surface, the 3D architecture allows for decoupling of the electrode distance from the device thickness. The results are a shorter drift path and consequently a faster charge collection as well as a lower voltage required for full depletion.

A silicon sensor with a three-dimensional electrode structure is shown in Fig. 3.3(a). In the case of silicon and other semiconductor devices, the electrodes are fabricated by etching trenches, e.g. via *deep reactive ion etching* (DRIE), into the bulk, subsequently doping these trenches and refilling them with polycrystalline material afterwards [19]. Therefore the technical fabrication for 3D electrodes is more complicated than for the standard planar electrodes.

Apart from the short drift distances in comparison to the detector thickness, as illustrated in Fig. 3.3(b) for a typical detector thickness in the region of the LHC experiments, 3D detectors also turned out to have an increased radiation hardness. Moreover, another

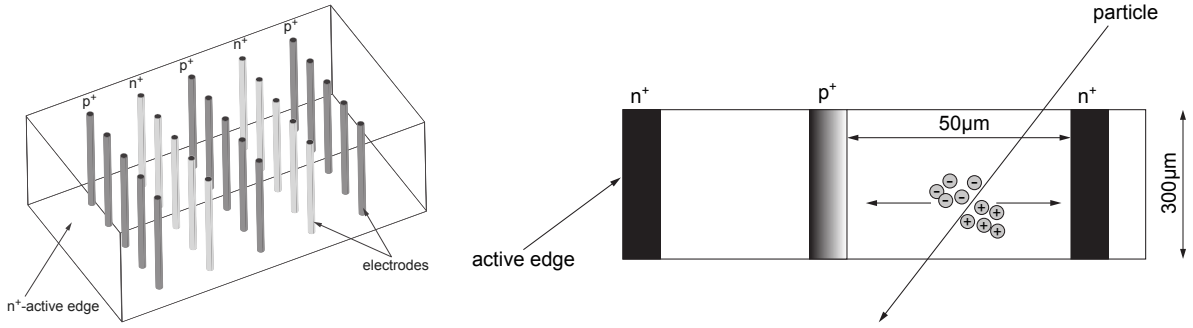

(a) (b)

Figure 3.3: (a) Schematic view of a 3D silicon detector; (b) charge collection 3D sensor with a thickness in the region of the LHC experiments and a typical electrode distance [9].

feature of this technology is the fact that the edge of the sensor can be employed as a collection electrode itself, hence extending the active area of the sensor to within about $10\,\mu$m to the edge [9]. One of the problems of 3D sensors, apart from the challenging fabrication, are the inefficient regions resulting from the columnar electrode structure, however, these are only relevant for particles traversing the material with exactly perpendicular trajectories.

The application of a similar technology is currently investigated for diamond detectors to avoid the problem of low CCD in pCVD material. However, in contrast to semiconductor devices, the main idea is to fabricate electrodes consisting of graphite, since this carbon allotrope is already conductive. Therefore one aims to locally convert the sp^3-bonds to sp^2, providing conductive channels within the material. This graphitisation can be achieved by infrared femtosecond laser pulses.

3.2.2 Graphitisation of CVD diamond

Theoretical [20–22] and experimental [23] studies have shown that diamond can be structured using intense femtosecond laser pulses. Moreover, Raman spectroscopy indicated that the fabricated structures consist of graphite. According to the underlying theory [20, 22], a dense electron-hole plasma is excited as a consequence of the interaction between the intense laser pulses and a semiconductor or insulator. During the resulting short-lived non-equilibrium situation, a phase transition from the metastable sp^3-bonded diamond to the stable sp^2-bonded graphite occurs in a non-thermal process.

The graphitisation of diamond can be used for several applications, e.g. surface graphitisation and ablation for laser polishing. However, the most attractive employment, with

regard to pCVD diamond detectors for particle physics, is the fabrication of conducting vias in the diamond bulk, which can be operated as electrodes for 3D pixel sensors.

In general, bulk graphitisation is achieved by focusing an IR femtosecond laser in the bulk. However, it has been shown [24] that irradiation not only yields graphitisation in the focus, but also that the graphite structure grows towards the incident beam in a conical shape, as shown in Fig. 3.4. The growth rate of the resulting graphite column in the case of a stationary focus decreases over the time of irradiation and its maximal length is limited by the laser power, especially in the case of relatively low power. In addition, the diameter of the latest generated part of the structure decreases approximately linearly with increasing irradiation time, consequently yielding a smaller diameter for lower growth rates [25].

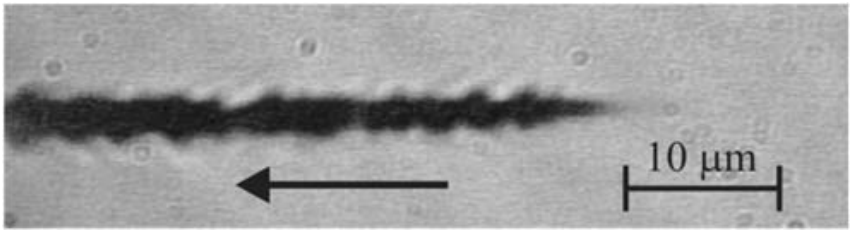

Figure 3.4: Continuous graphitisation at an incident beam power of 210 μW with the stationary focus coinciding with the left border of the figure and the arrow indicating the direction of irradiation. Repetitive irradiation results in a growth whose direction is opposite to the arrow [25].

Considering these facts regarding continuous graphitisation, longitudinal graphite structures are best fabricated by uniform motion of the focus in the bulk. For perpendicular graphite columns in the bulk, the focus is usually positioned behind the surface at first, such that no graphitisation occurs, and is subsequently moved towards the irradiating beam at constant speed. Similarly to the cone diameter being dependent on the growth rate in the case of a stationary focus, the graphite diameter depends on the speed of the focus. As a result – albeit unintuitive – lower speed yields smaller diameters, which is illustrated in Fig. 3.5(a).

However, the shape and diameter of the structures not only depend on the growth rate, but also directly on the laser power. A larger laser power leads to additional breakdown of the diamond structure in an extended area around the focus point. Consequently, the occurrence of breakdown is no longer controllable and irregularities appear in the graphitisation [24, 25]. Apart from this effect, the overall diameter of the graphite columns also increases with the laser power. This behaviour is shown in Fig. 3.5(b).

As conclusion, the writing of longitudinal structures is best controlled by laser powers

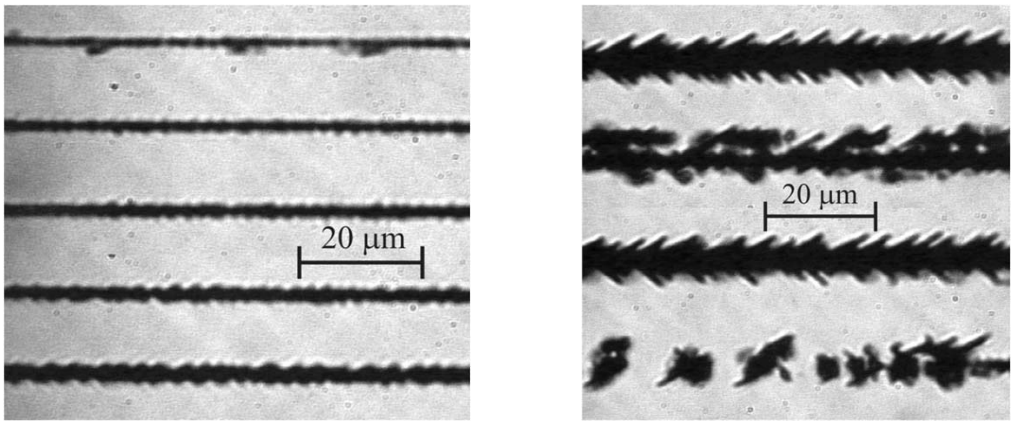

(a) (b)

Figure 3.5: Graphitised traces written with (from top to bottom) (a) 210 μW laser power with speeds from 1 μ/s to 30 μ/s and (b) 1.53 mW with speeds from 30 μ/s to 100 μ/s; the width of the traces is in (a) 1.5 μm, 2 μm, 2.5 μm, 3 μm, 3.5 μm, respectively and in (b) about 10 μm each [25].

only slightly above the graphitisation threshold and a speed adjusted to the intended electrode diameter. It has already been shown that this process is in general a reliable method to fabricate 3D structures in diamond bulk with varying distances to one another, as it can be seen in Fig. 3.6, therefore being adaptable to different requirements.

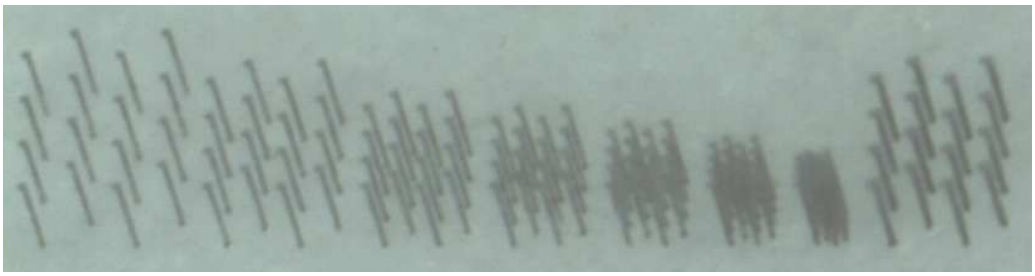

Figure 3.6: Graphitised columns in diamond with varying distance and thickness [26].

4 C-V measurements

The measurement of the voltage-dependent capacitance of a semiconductor device, e.g. a diode or MOSFET, is a basic method of characterisation. It is used to determine quantities such as the effective dopant concentration and full depletion voltage. In this thesis, the results obtained with these measurements are also used in comparison to the respective measurements with the transient current technique (see chapter 5). Furthermore, the capacitance of the measured silicon diode itself is important for the calculation of the underlying current pulse in TCT measurements.

4.1 Basics of C-V measurements

The definition of capacitance at a given voltage U_0 is

$$C(U_0) = \left.\frac{\mathrm{d}Q}{\mathrm{d}U}\right|_{U=U_0} = \left.\frac{\mathrm{d}Q}{\mathrm{d}w}\frac{\mathrm{d}w}{\mathrm{d}U}\right|_{U=U_0} \tag{4.1}$$

with w being the distance between the respective electrodes. In the case of a p-n junction w is the width of the depletion zone. Additionally, the space charge of the diode can be defined as $Q = eN_{\mathrm{eff}}Aw$ where A is the area of the p-n junction and N_{eff} the effective space charge concentration (see section 2.3.1). Assuming an applied external reverse bias voltage U, with $U_{\mathrm{FD}} > U \gg U_{bi}$, the respective depletion depth is described by Eq. 2.15 and $\frac{\mathrm{d}w}{\mathrm{d}U} = \sqrt{\frac{e\varepsilon_{\mathrm{r}}\varepsilon_0}{2eN_{\mathrm{eff}}U}}$. For $U \geq U_{\mathrm{FD}}$ the depth of the depletion zone equals the thickness D of the diode.

Considering the case of an abrupt p-n junction and neglecting any edge effects, the capacitance of the diode is

$$C(U) = \begin{cases} \frac{\varepsilon_{\mathrm{r}}\varepsilon_0 A}{w} = \sqrt{\frac{e\varepsilon_{\mathrm{r}}\varepsilon_0 N_{\mathrm{eff}}}{2U}}A & , U < U_{\mathrm{FD}} \\ \frac{\varepsilon_{\mathrm{r}}\varepsilon_0 A}{D} & , U \geq U_{\mathrm{FD}} \end{cases} \tag{4.2}$$

With respect to this dependence it is apparent, that in the case of reverse bias and constant N_{eff} over the detector thickness, the graph of $C^{-2}(U)$ versus U yields a straight

line below the full depletion voltage U_{FD} and a constant value for higher voltages. Thus the kink of the graph yields U_{FD} and the effective doping concentration can be determined either by the slope

$$\frac{\mathrm{d}\left(C^{-2}(U)\right)}{\mathrm{d}U} = \frac{2}{e\varepsilon_0\varepsilon_r N_{\mathrm{eff}} A^2} \tag{4.3}$$

for a voltage $U < U_{\mathrm{FD}}$ or from the depletion voltage via

$$N_{\mathrm{eff}} = \frac{2\varepsilon_r\varepsilon_0 U_{\mathrm{FD}}}{eD^2} \tag{4.4}$$

The same relations are also valid for sensor materials other than semiconductors with their respective properties, such as diamond.

4.2 Experimental setup

In order to measure the capacitance of various samples, a B1505A Power Device Analyser from *Agilent Technologies* has been employed. The samples themselves are mounted to a simple circuit board and subsequently contacted via wirebonds. The board is located inside a sheet metal box, which acts as a Faraday cage, hence reducing electromagnetic pick-up, and as a protection against ambient light.

4.2.1 Silicon diode sample

The sample *6134-15-17* is an unirradiated p-in-n silicon diode. A picture of the sample is shown in Fig. 4.1(a). This diode along a batch of similar diodes, which originate from the same wafer and were equally fabricated, have been used for C-V and TCT (see chapter 5) measurements during the course of this work.

The diode is processed by implanting highly doped p-type silicon in n-type silicon substrate. The sensitive material on both sides of the diode, the n-side as well as the p-side, are protected by a SiO_2 passivation layer. In order to contact the diode, aluminium electrodes are implemented on the surface on both sides. Leakage current at the sensor edges is avoided by the usage of a guard ring structure.

The diode surface is quadratic and exhibits an area of $6 \times 6\,\mathrm{mm}^2$. The area of the electrodes on the p-side is approximately $3.5 \times 3.5\,\mathrm{mm}^2$ with a $1.5 \times 1.5\,\mathrm{mm}^2$ hole in the passivation layer. On the n-side, the size of the electrodes is $3 \times 3\mathrm{mm}^2$ with a $1.5 \times 1.5\mathrm{mm}^2$ hole. The thickness of the diode is 250 μm.

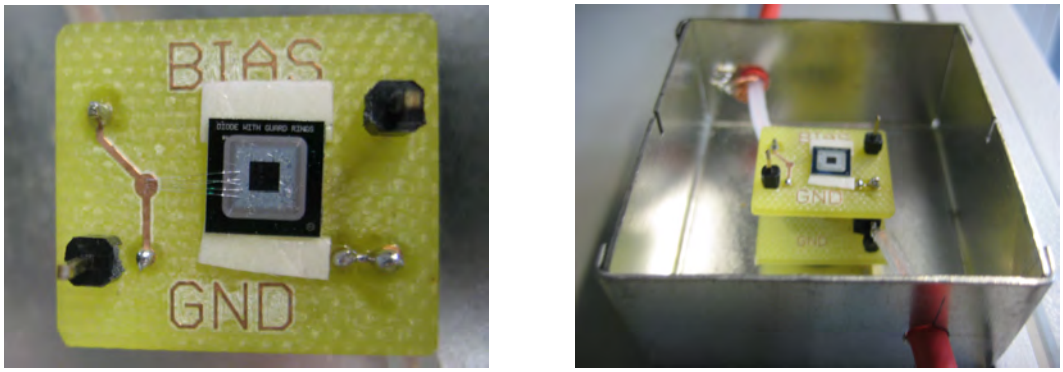

(a) (b)

Figure 4.1: (a): p-side of the silicon diode used for C-V measurements. The diode is connected to the board via wirebonds. (b): board with DUT plugged in to the DUT mount inside the metal box.

4.2.2 The DUT mount

A picture of a mounted and contacted silicon diode sample inside the metal box can be seen in Fig. 4.1(b). A plastic block is used as a fixture of the board. The board itself provides insulation against the box, therefore the box acts as a Faraday cage. The diode itself is contacted via wirebonds on a separate board, which is designed to be easily interchangeable and rotatable in order to allow measurements with positive as well as negative sign of bias voltage.

Moreover, as silicon diodes under reverse bias also act as photodiodes, thus being a current source under irradiation, the box is necessary to protect the DUT from ambient light. Similarly, UV light unpumps the defect states of diamond, hence alters the measurement.

4.2.3 The B1505A Power Device Analyser

The capacitance C of a *device under test* (DUT) cannot be measured directly, unlike e.g. current or voltage. In general, it is determined from the complex impedance by measuring the amplitude and phase shift of a signal in the DUT in response to an AC measuring voltage with

$$Z = R + \mathrm{i}\left(2\pi f L - \frac{1}{2\pi f C}\right) \tag{4.5}$$

where R and L are the resistivity and inductance of the DUT respectively, and f the frequency of the applied AC measurement voltage. Additionally, a DC voltage is applied in order to bias the device.

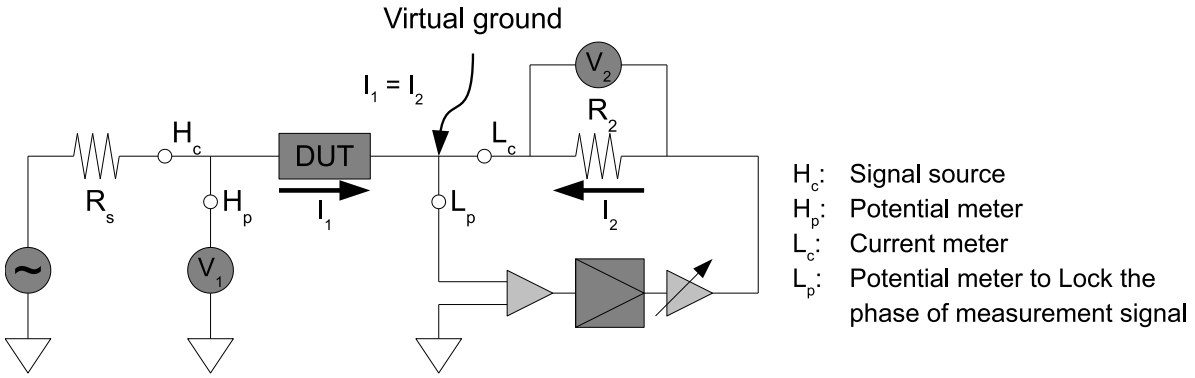

Figure 4.2: Schematic circuit of the auto balancing bridge capacitance measurement method [27].

The used method of capacitance meter operations is the *auto balancing bridge*, as shown in Fig. 4.2. The bridge itself can be conceptualised as an operational amplifier circuit. The AC signal, which is used to stimulate the device, is monitored at the H (high) terminal along with the DC bias U_1, whereas the L (low) terminal is driven to 0 V by the virtual ground of the operational amplifier. Thus, the current I_2 through the resistor R_2 is equal to the current through the DUT I_1. Therefore, the output voltage U_2 is proportional to the current through the DUT and voltages and currents are automatically balanced. Applying Ohm's law yields the impedance of the device as

$$Z_{\mathrm{DUT}} = \frac{U_1}{I_1} = \frac{U_1}{I_2} = \frac{U_1 R_2}{U_2} \tag{4.6}$$

The complex impedance of a device also leads to a phase shift φ between voltage and current:

$$\tan\varphi = \frac{\mathrm{Im}\ Z}{\mathrm{Re}\ Z} = \frac{\omega L - \frac{1}{\omega C}}{R} \tag{4.7}$$

with $\omega = 2\pi f$. The capacitance of the device can be calculated from Eq. 4.5 by using the measurement results in combination with Eqs. 4.6 and 4.7.

The auto balancing bridge is implemented in the B1505A using the *4 terminal pair* (4TP) measurement method. In this procedure, the high (H_c and H_p in Fig. 4.2) and low (L_c and L_p) are shorted together. Thus the DUT inside the box only needs to be connected by two SHV cables. The *Capacitance Measurement Unit* (CMU) of the instrument allows measurements in the frequency range from 1 kHz to 5 MHz with DC bias voltages up to ±3000 V due to the high-voltage *Source/Monitor Unit* (SMU) of the B1505A. The AC voltage amplitude can be set from 10 mV to 250 mV. The necessary cabling is provided by

the N1260A High-Voltage Bias-Tee, which in conjunction with the aforementioned CMU and HVSMU allows for precise high-voltage capacitance measurements with minimal additional work regarding the test fixture.

An important aspect for high precision in C-V measurements are compensation measurements for the parasitic effects of the cabling and connections, which are conducted with opened and shorted terminals. Thus residual impedances and stray admittances of the measurement setup without the DUT can be automatically taken into account by the instrument. Also measurement errors due to these parasitic effects are reduced.

4.3 Results

4.3.1 Selection of measurement parameters

Since the instrument allows for a number of measurement parameters to be selected beforehand, the optimal choice of these parameters is crucial for precise capacitance measurements. In this case, the most important parameters are the frequency of the AC measurement voltage and the respective amplitude.

In order to yield a measure on the impact of the selected measurement frequency, the silicon diode is measured at a constant bias $U = 100\,\mathrm{V}$, which is well above the assumed full depletion voltage $U_{\mathrm{FD}} \approx 60\,\mathrm{V}$ as seen in previous measurements. Since the programme of the B1505A does not allow a measurement at an actual constant voltage, a 1 mV sweep in the range from 99.9995 V to 100.0005 V with an increment of 1 μV is performed. Thus the measurement is repeated 1001 times, which improves statistics, with a time interval of 500 ms between each consecutive measurement to minimise the effect of circuit switching in the bias supply.

Verification that such a measurement indeed equals a measurement at constant bias is shown in Fig. 4.3, in which the bias voltage of each step is filled into a histogram. The distribution exhibits a Gaussian shape, which is subsequently fitted using ROOT and MINUIT, with a mean value of 100 V and a standard deviation of $9.8 \pm 0.3\,\mathrm{mV}$. Therefore, the deviation from of the bias voltage due to the uncertainty of the high voltage supply is about one order of magnitude larger than the actual sweep. Thus the effect of the sweep on the capacitance measurement is negligible and one can consider the measurement to be conducted at fixed bias.

The exemplary results of such a measurement at fixed bias $U_{\mathrm{bias}} = 100\,\mathrm{V}$ are shown in Fig. 4.4 as the recorded capacitance values plotted versus the measurement time. The mean capacitance is determined by the fit of a constant to the data points. Shown error

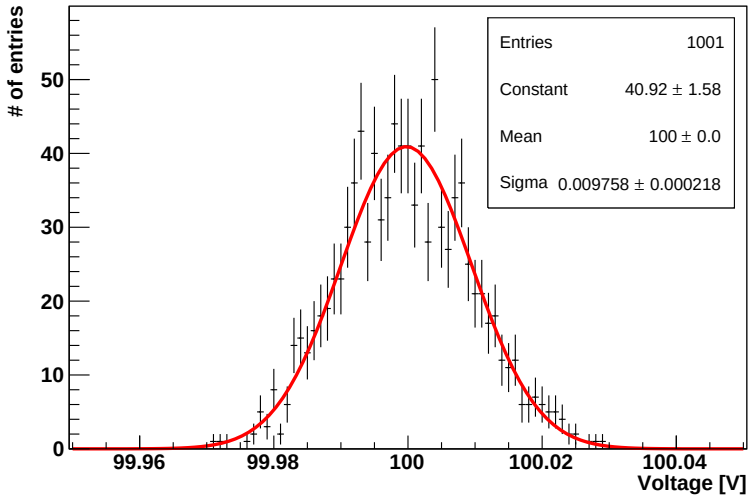

Figure 4.3: Distribution of the DC bias voltage measured during capacitance measurement at a fixed bias voltage of 100 V with the AC measurement voltage featuring an amplitude of 250 mV and a frequency of 200 kHz. Errors shown in the histogram account for Poisson uncertainties in the respective bins.

bars represent the systematic uncertainties, calculated for each point according to [28]. The statistical uncertainty is given by the RMS of the mean value.

Accordingly, the measurement is repeated for a representative selection of AC oscillation frequencies, the results of which are displayed in Tab. 4.1.

frequency	capacitance [pF]	stat. uncertainty [pF]	syst. uncertainty [pF]
1 kHz	10.3	1.2	0.4
5 kHz	9.7	0.3	0.1
10 kHz	9.50	0.08	0.05
50 kHz	8.81	0.02	0.03
100 kHz	8.550	0.004	0.017
200 kHz	8.371	0.002	0.016
500 kHz	7.986	0.003	0.016
1 MHz	7.518	0.006	0.015
5 MHz	6.425	0.004	0.034

Table 4.1: Mean values of device capacitance for different frequencies at a measurement voltage amplitude of 250 V and with fixed bias of 100 V.

It can be seen that there is a discrepancy between the results for the different frequencies. These variations originate most likely in the existence of stray inductance, and thus additional impedance especially for high frequencies, which leads to a deviation from the simple RC model of a p-n junction. Fig. 4.5 shows the equivalent circuit for such a

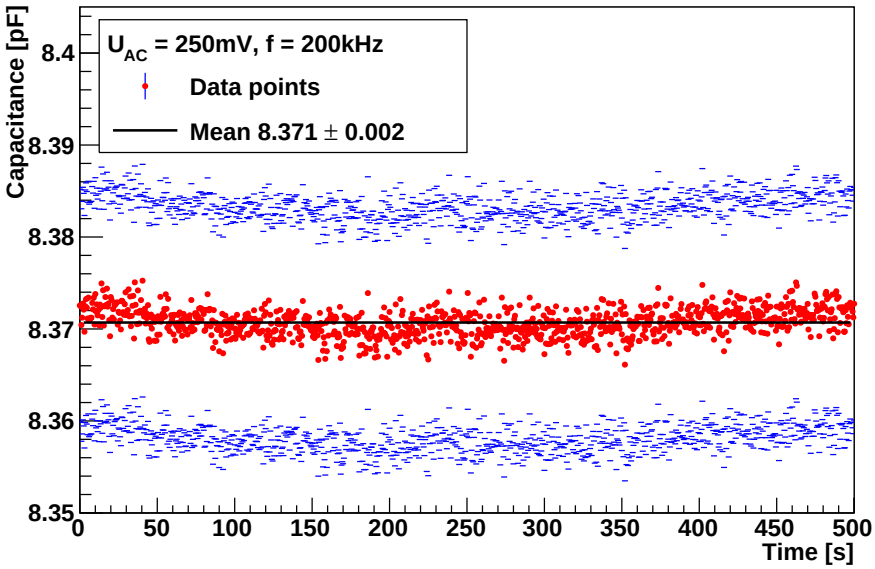

Figure 4.4: Measured capacitance of the silicon diode versus measurement time at a bias voltage of 100 V with the AC measurement voltage featuring an amplitude of 250 mV and a frequency of 200 kHz. The ends of the error bars (blue bands) correspond to the respective systematic uncertainty, the error given for the mean value is the statistical uncertainty.

model of a partially biased diode, with a parallel capacitor and resistor accounting for the resistance and capacitance of the depleted (*dep*) and undepleted bulk (*bulk*) regions respectively, in addition to a resistor for surface currents. At low bias voltages the capacitance of the depletion zone dominates, since the differential resistivity ($R_{\mathrm{dep}} = \frac{\mathrm{d}U}{\mathrm{d}I} \gg \omega C_{\mathrm{dep}}$) of a reversely biased diode is high, whereas the undepleted bulk can be described by the resistor alone ($R_{\mathrm{bulk}} \ll \omega C_{\mathrm{bulk}}$). At voltages close to the full depletion voltage, the sensor bulk can be described by a single capacitor parallel to the surface resistor. Hence higher measurement frequencies indicate the increasingly dominant contribution of capacitances in impedances of the depleted and undepleted regions of the device. Furthermore, higher oscillation frequencies are more susceptible to deviations from this model by introducing stray impedances. Thus the overall measured impedance according to Eq. 4.5 would be larger for higher frequencies due to the unaccounted inductances, resulting in lower capacitances.

With regards to these results, the AC oscillation frequency of choice for subsequent capacitance measurements is 200 kHz, mainly because of the low statistical and systematic uncertainty, but also because additional deviations of the capacitance with time have been observed for higher frequencies.

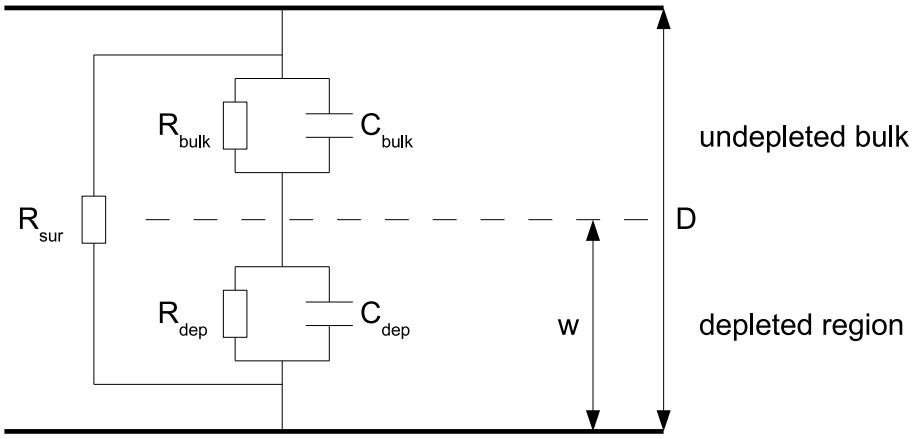

Figure 4.5: Equivalent circuit of a partially depleted diode in a simple RC model. Depletion region and undepleted bulk are connected in series and are modelled by a parallel capacitor and resistor each. An additional parallel resistor accounts for surface current (sketch redrawn from [10]).

In analogy to the measurements for different frequencies, the amplitude of the oscillations has also been varied for measurements at a fixed bias of $U_{\text{bias}} = 100$ V. The results can be seen in Tab. 4.2. The mean capacitance for the selected amplitudes is in good agreement with each other within the statistical and systematic uncertainty. In conclusion, the best measurement parameter in order to provide a stable measurement with minimal uncertainties is an AC frequency of 200 kHz with an amplitude of 250 mV. The measured capacitance corresponds to an area of the p-n junction of approximately $(4.46 \times 4.46 \pm 0.04)$ mm^2. This is in agreement with the sample dimensions considering the fact that the p-n junction also extends below the guard rings and the hole in the passivation.

amplitude	capacitance [pF]	stat. uncertainty [pF]	syst. uncertainty [pF]
10 mV	8.36	0.03	0.05
20 mV	8.36	0.02	0.03
50 mV	8.364	0.006	0.018
100 mV	8.368	0.003	0.017
200 mV	8.370	0.002	0.017
250 mV	8.371	0.002	0.016

Table 4.2: Mean values of device capacitance for different amplitudes of the oscillation at a measurement frequency of 200 kHz and with fixed bias of 100 V.

4.3.2 C-V sweep

To determine the characteristic quantities of the silicon diodes used in the TCT setup, a voltage sweep has been performed. The capacitance of the diode has been measured in the DC bias voltage range from 0 V to 140 V at reverse bias with AC measurement parameters $U_{AC} = 250\,\text{mV}$ and $f = 200\,\text{kHz}$ as mentioned in the previous section. The results of the voltage sweep are shown in Fig. 4.6. As before, errors are calculated from the systematic uncertainty, however, the error bars are too small to be seen.

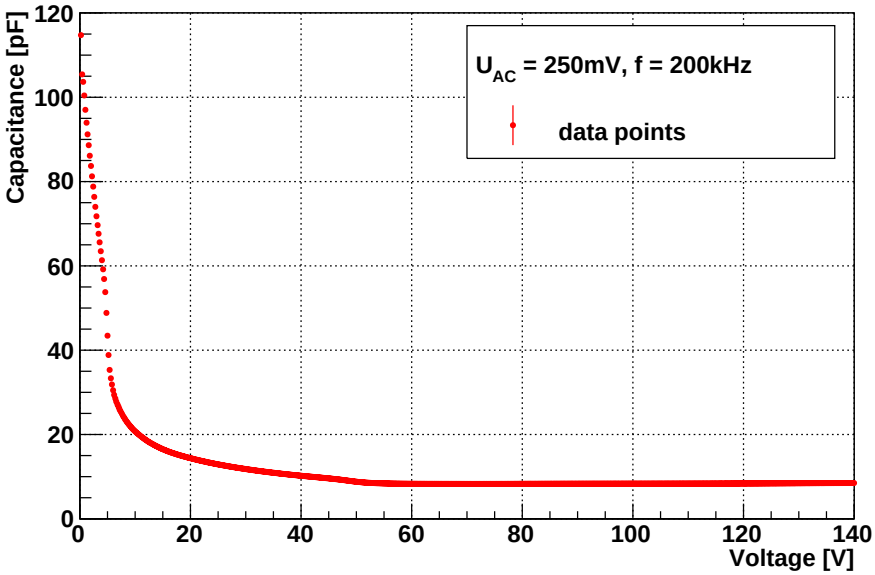

Figure 4.6: Capacitance versus bias voltage for the silicon diode used to characterise the TCT setup. Error bars are present but too small to be seen.

The measured capacitance is in good agreement with the expected general behaviour as described in section 4.1. The capacitance decreases with increasing bias, resulting in an approximately constant capacitance for high bias voltages. An additional feature, which can be seen, is a slight kink and hence a change in the overall behaviour at a bias $U \approx 5\,\text{V}$. This effect occurs most likely due to the punch-through biasing of the guard rings (see section 2.3.1) and the subsequent depletion of the small p-n junctions between the rings, similar to the observed behaviour of strip detectors [29].

In order to determine the full depletion voltage and the effective doping concentration, $1/C^2$ has been plotted versus the bias voltage. The plot is shown in Fig. 4.7.

The most prominent feature observable in the figure is the kink which is used in the following to determine the full depletion voltage. Additionally, the already mentioned second, smaller kink at $U \approx 5\,\text{V}$ can be seen more clearly.

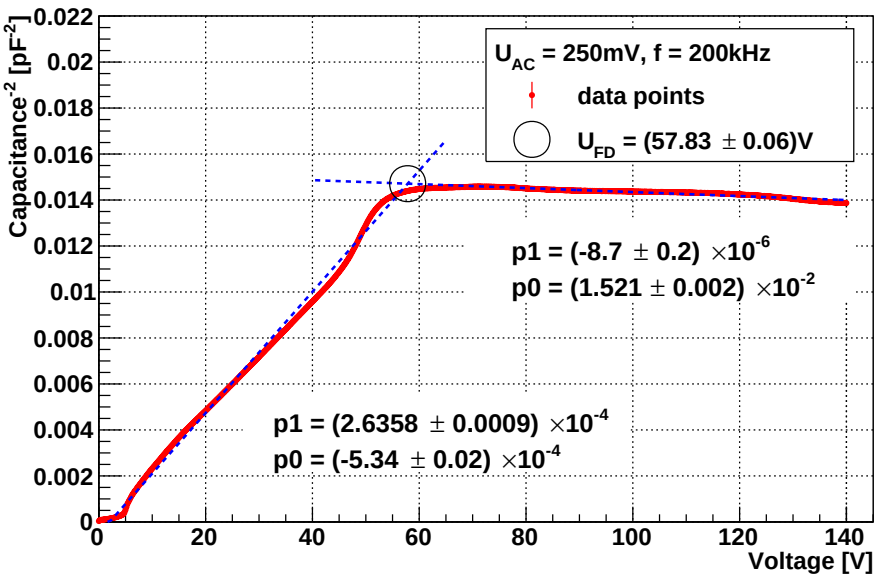

Figure 4.7: $1/C^2$ versus bias voltage of the silicon diode. Linear fits, the respective fit results, and the resulting full depletion voltage are shown. Error bars are too small to be seen.

Linear functions $C^{-2} = p0 + p1 \cdot U$ have been fitted to the linear parts of the curve before and after the apparent kink in the plot, with the intersection of the functions yielding a full depletion voltage of $U_{\mathrm{FD}} = (57.83 \pm 0.06)$ V. 5 V to 55 V has been chosen as the fit range for voltages $U < U_{\mathrm{FD}}$, in order to avoid the deviations at low bias. For the upper voltage range, 65 V to 140 V has been selected to determine the second linear function. The uncertainty given for U_{FD} is derived from the uncertainties of the fit parameters. An additional systematic uncertainty is introduced by the choice of the fitting range. Varying the range leads to $\Delta U_{FD}(\mathrm{syst.}) = 0.5$ V. This result for the full depletion voltage agrees well with the observations from previous measurements

The effective doping concentration N_{eff} has been calculated using Eq. 4.3 and the slope of the linear fit for bias below U_{FD} as well as via U_{FD} and Eq. 4.4. The result for the former method is $N_{\mathrm{eff}} = \left(1.217 \pm 0.002(\mathrm{stat.}) \pm 0.023(\mathrm{syst.})\right) \times 10^{12}\,\mathrm{cm}^{-3}$, the latter method yields $N_{\mathrm{eff}} = \left(1.136 \pm 0.005(\mathrm{stat.}) \pm 0.011(\mathrm{syst.})\right) \times 10^{12}\ \mathrm{cm}^{-3}$. The quoted uncertainties are calculated from the uncertainties of the underlying quantities hence including systematic uncertainties from the variation of the fitting range. Within the margin of the respective uncertainties, these values differ slightly from each other, however, only on a per cent level.

5 Transient Current Technique

The following sections describe the physics of signal formation in a detector material with regard to the aspects of the transient current technique. This technique is a very powerful tool, able to measure several electrical properties of semiconductors or insulators. Therefore an application to diamond samples is of interest.

5.1 Charge carrier transport and induced signals

The transport of charge carriers in a material can occur via *drift* or *diffusion*.

Diffusion originates from Brownian motion further directed by differences in concentration and is a thermally driven statistical random-walk. As a result, a local δ-distributed charge carrier concentration spreads to a Gaussian. The width σ of the corresponding Gaussian distribution depends on time and is defined by the material-dependent *diffusion constant* $\mathcal{D}$ with

$$\sigma = \sqrt{\mathcal{D}t} \tag{5.1}$$

Charge carrier drift requires the presence of an electric field. In contrast to the typically accelerated movement of charge carriers in an electric field, continuous energy transfer by scattering off atoms in the crystal lattice yields an additional deceleration and results in a net constant *drift velocity* $\vec{v}_D$ within the material. The drift velocity is usually described by the respective charge carrier mobility $\mu_{e,h}$ and depends on the electric field:

$$\vec{v}_D = \mu\vec{E} \tag{5.2}$$

Drift and diffusion in thermal equilibrium are connected by the *Einstein relation* [30]:

$$\mathcal{D}_{e,h} = \frac{k_B T}{e}\mu_{e,h} \tag{5.3}$$

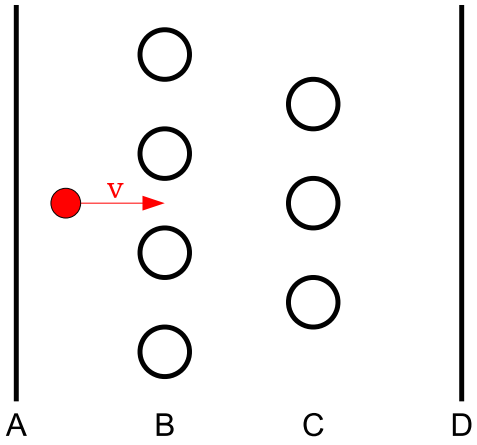

Figure 5.1: Illustration of a number of electrodes A, B, C, D of a grid in the presence of a moving charge whose path $\vec{r}(t)$ and instantaneous velocity v are known (figure redrawn from [31]).

Shockley-Ramo theorem

The general derivation of induced currents on electrodes originating from the drift of mobile charges in an electric field can be very difficult with increasing complexity of the underlying setup. Additionally, in the case of charge carriers with relatively long transit times, the low-frequency concept of instantaneous current, taken by the electrode once the charge reaches the electrode and hence a proportionality of the induced current to the number of electrons received, has to be discarded. Moreover, electrodes may carry current even though they collect no charges at all and current can be noted during the time the charges are still approaching the electrodes. A simple method of computing the induced current for a specified electron motion has been shown in a work by Simon Ramo [31].

One considers a charge e, say an electron, in the presence of any number of grounded electrodes (as illustrated in Fig. 5.1), for one of which, say A, the induced current has to be derived. A tiny equipotential sphere of the electrostatic potential ϕ_e around the electron can hence be assumed, however, the overall potential on the electrode is $\phi = 0$ and the region between electrodes is described by

$$\nabla^2 \phi = 0 \tag{5.4}$$

The charge on the surface of the sphere according to Gauss' Law is

$$-\int_{\text{sphere's surface}} \nabla\phi \cdot \mathrm{d}\vec{S} = 4\pi e \tag{5.5}$$

The next step is to consider the same set of electrodes with the electron removed and electrode A raised to unit potential, whereas the others are still grounded. Thus one can assume the potential of the resulting field to be ϕ', such that $\nabla^2\phi' = 0$ is still valid in the region between electrodes, including the point where the electron has once been. The potential at the former electron position $\vec{r}_e$ is denoted $\phi'_e = \phi'(\vec{r}_e)$.

Applying *Green's theorem* according to [32] leads to

$$\int_V \left[\phi'\left(\nabla^2\phi\right) - \phi\left(\nabla^2\phi'\right)\right] \mathrm{d}V = \int_S \left[\phi'\left(\nabla\phi\right) - \phi\left(\nabla\phi'\right)\right] \cdot \mathrm{d}\vec{S} \tag{5.6}$$

with the first integral over the volume between boundaries and the second over the respective boundary surfaces. Choosing the boundary conditions such that the volume is bounded by the electrodes and the tiny equipotential sphere yields the left-handed side to be zero and the right-handed side to be divided in three separate integrals:

1. The integral over the surface of all electrodes except for A. Since $\phi = \phi' = 0$ on these surfaces, the integral is zero.

2. Integrating over the surface of A can be reduced to $-\int_{\text{surface A}} \nabla\phi \cdot \mathrm{d}\vec{S}$ with $\phi = 0$ and $\phi' = 1$ for electrode A

3. For the integral over the surface of the equipotential sphere, one can replace the right-handed side of Eq. 5.6 with

$$-\phi'_e \int_{\text{sphere's surface}} \nabla\phi \cdot \mathrm{d}\vec{S} + \phi_e \int_{\text{sphere's surface}} \nabla\phi' \cdot \mathrm{d}\vec{S}$$

   where the second integral is zero by Gauss' law due to the removal of the electron.

As conclusion, Green's theorem yields

$$0 = -\int_{\text{surface A}} \nabla\phi \cdot \mathrm{d}\vec{S} - \phi'_e \int_{\text{sphere's surface}} \nabla\phi \cdot \mathrm{d}\vec{S} = 4\pi Q_A + 4\pi e\phi'_e \tag{5.7}$$

or accordingly

$$\begin{aligned} Q_A &= -e\phi'_e \\ \Longrightarrow\ I_A &= \frac{\mathrm{d}Q_A}{\mathrm{d}t} = -e\frac{\mathrm{d}\phi'_e}{\mathrm{d}t} = -e\left[\nabla\phi'_e \cdot \frac{\mathrm{d}\vec{r}_e}{\mathrm{d}t}\right] \end{aligned} \tag{5.8}$$

with the trajectory of the drifting charge $\vec{r}_e(t)$ being a solution to the equation of motion

in an electric field $\vec{E}(\vec{r})$

$$\frac{\mathrm{d}\vec{r}_e}{\mathrm{d}t} = v_D(\vec{r}_e) = \mu\vec{E}(\vec{r}_e) \qquad \text{and} \qquad \nabla\phi'_e = \nabla\phi'|_{\vec{r}=\vec{r}_e} = -\vec{E}_w(\vec{r}_e) \tag{5.9}$$

where $\vec{E}_w$ is the *weighting field* with potential ϕ'. The weighting potential is obtained by solving the Laplace equation under the boundary conditions of its definition ($\phi' = 1$ at the surface of electrode A, $\phi' = 0$ for any other electrode).

Hence the general equation describing a current, induced on an electrode by a charge q moving in an electric field with velocity v_D, is the *Shockley-Ramo theorem*:

$$I_{\mathrm{ind}} = q\vec{E}_w(\vec{r}(t)) \cdot \vec{v}_D(\vec{r}(t)) \tag{5.10}$$

Charge trapping

Charges can be trapped during drift in a material. This effect becomes even more important in the case of diamond sensors or semiconductor devices after operation in high-radiation environments. The drift velocity of trapped charges becomes zero, hence they do not contribute to the induced current anymore according to Eq. 5.10. The probability of a charge being trapped is proportional to the traversed length in the material represented by the *effective carrier trapping distance* $\lambda_{e,h}$. Since the thermal velocity $v_{th_{e,h}}$ of charge carriers is typically much larger than the drift velocity, this quantity can be expressed as the *effective carrier trapping time* $\tau_{e,h} = \lambda_{e,h}/v_{th_{e,h}}$. Consequently, the number of charge carriers exhibit an exponential behaviour over time [10]:

$$\mathrm{d}N = -N_0 \cdot \frac{1}{\lambda_{e,h}}\mathrm{d}l = -N_0 \cdot \frac{1}{\tau_{e,h}}\mathrm{d}t \quad \Longrightarrow \quad N(t) = N_0 \cdot \exp\left(-\frac{t}{\tau_{e,h}}\right) \tag{5.11}$$

5.1.1 Signal formation in silicon detectors

Assuming the case of a silicon pad detector composed of two parallel electrodes with lateral dimensions much larger than the detector thickness D, a constant weighting field $E_w = -1/D$ is obtained [31]. An induced current due to the drift of electrons and holes can thus be described by

$$I_{e,h}(t) = -\frac{eN(t)}{D}v_D(t) \tag{5.12}$$

with N being the number of drifting charge carriers and v_D the drift velocity. The latter requires the knowledge of the electric field profile in the detector. In the case of an

overdepleted detector ($U > U_{\mathrm{FD}}$) the electric field usually exhibits a linear behaviour [10]:

$$E(x) = \frac{1}{D}\left(U - z\left(1 - \frac{2x}{D}\right)U_{\mathrm{FD}}\right) \tag{5.13}$$

where z denotes the sign of the space charge in the depletion zone. Using the approximation of constant mobility $\mu_{e,h}(E) \approx \mu_{0_{e,h}}$, which is valid for moderate field strengths, an analytical expression for the induced current can be found. Rewriting Eq. 5.9 as

$$\frac{\mathrm{d}x_{e,h}(t)}{\mathrm{d}t} = \mp\mu_{0_{e,h}} E(x) \tag{5.14}$$

and inserting Eq. 5.13 yields a solution for the equation of motion as follows [10]:

$$x_{e,h}(t) = \frac{zU - U_{\mathrm{FD}}}{2U_{\mathrm{FD}}} D\left[\exp\left(\frac{\mp zt}{\tau_{\mathrm{eff}_{e,h}}}\right) - 1\right] + x_0 \exp\left(\frac{\mp zt}{\tau_{\mathrm{eff}_{e,h}}}\right) \tag{5.15}$$

$$\tau_{\mathrm{eff}_{e,h}} = \frac{D^2}{2U_{\mathrm{FD}}\mu_{0_{e,h}}} = \frac{\varepsilon_{\mathrm{Si}}\varepsilon_0}{e\mu_{0_{e,h}}\left|N_{\mathrm{eff}}\right|} \tag{5.16}$$

in which x_0 is the starting point of the drift and $\tau_{\mathrm{eff}_{e,h}}$ the *transient time* of electrons and holes, respectively. The resulting drift velocity is hence

$$v_{D_{e,h}}(t) = \mu_{0_{e,h}}\left[\frac{U - zU_{\mathrm{FD}}}{D} + \frac{2zx_0U_{\mathrm{FD}}}{D^2}\right]\exp\left(\frac{\mp zt}{\tau_{\mathrm{eff}}}\right) = \mu_{0_{e,h}} E\left(x_0\right)\exp\left(\frac{\mp zt}{\tau_{\mathrm{eff}_{e,h}}}\right) \tag{5.17}$$

As conclusion, the current can be calculated with respect to Eqs. 5.11, 5.12 and 5.17 as

$$I_{e,h}(t) = \frac{eN(t=0)}{D}\mu_{0_{e,h}} E\left(x_0\right)\exp\left(\frac{\mp zt}{\tau_{\mathrm{eff}_{e,h}}} - \frac{t}{\tau_{e,h}}\right) \tag{5.18}$$

5.2 Basics of TCT measurements

The *transient current technique* (TCT) is based on the observation of current pulses, induced on the electrodes of the sample detector by the drift of free charge carriers in an electric field within the detector. The charge carriers can be generated in the active region of the detector by short laser pulses – usually in the case of semiconductors – or ionising radiation, such as α particles. Their drift induces current signals on the electrodes according to Ramo's theorem (Eq. 5.10). Assuming the case of silicon pad detectors, as derived in Section 5.1.1, the induced current is described by Eq. 5.18, provided the approximation of constant mobility and linear electric field holds.

In general, electron-hole pairs are injected across the whole detector volume, thus the

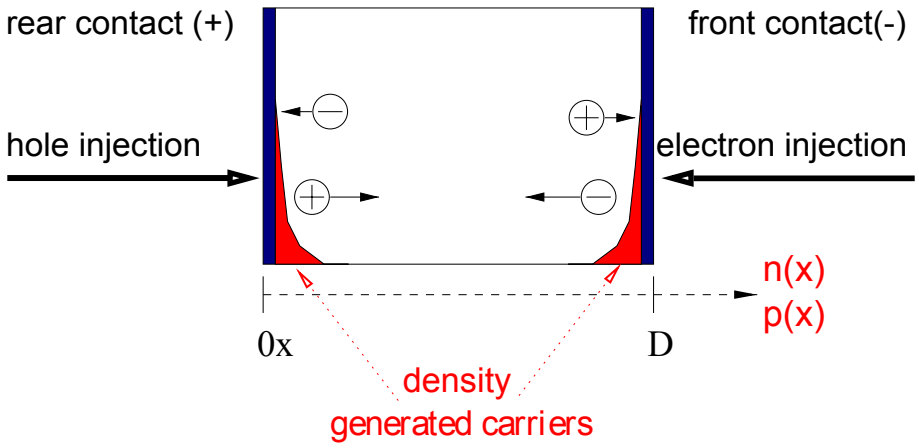

Figure 5.2: Schematic principle of TCT measurements, charge carrier injection with spatial density of generated carriers (red) according to Eq. 5.19 [10].

induced current is the sum of both contributions for electrons and holes $I(t) = I_h(t)+I_e(t)$. However, for TCT measurements one usually aims to generate charge carriers at small depths below the electrodes to measure only one type of charge carrier at a time. Provided N_{e-h} electron-hole pairs are created in the vicinity of one contact of the fully depleted detector, as shown in Fig. 5.2, one type of carrier will move across the whole detector length, whereas the complementary carrier type is collected immediately by the adjacent electrode. The result is a nearly exclusive generation of electrons or holes, referred to as *electron* and *hole injection*, yielding a separate measurement of corresponding signal pulses for the particular charge carrier type. Therefore either α particles or a laser wavelength for which the detector material has a high absorption coefficient are used for charge generation. Since the charge carriers are not generated at an infinitesimal distance from the electrodes but exhibit an exponential behaviour, the spatial distribution can be described as follows:

$$n(x, t=0) = p(x, t=0) = \frac{N_{e-h}}{\alpha_{abs} A_i} \begin{cases} \exp\left(-\frac{D-x}{\alpha_{abs}}\right) & \text{electron injection} \\ \exp\left(-\frac{x}{\alpha_{abs}}\right) & \text{hole injection} \end{cases} \qquad x \in [0, D] \quad (5.19)$$

where A_i is the illuminated area, α_{abs} the absorption length and D the detector length.

An example of measured current pulses in a silicon detector with several key features of TCT signals is shown in Fig. 5.3 for both electrons and holes as well as different applied bias voltages [10]. The different scaling of the x-axis (time) has to be noted at first, hence the hole pulses exhibit a much larger pulse width as expected because of the smaller hole mobility. Moreover, the pulse shape provides information about the electric field in the material. The decrease during the electron pulse indicates a high electric field region at the

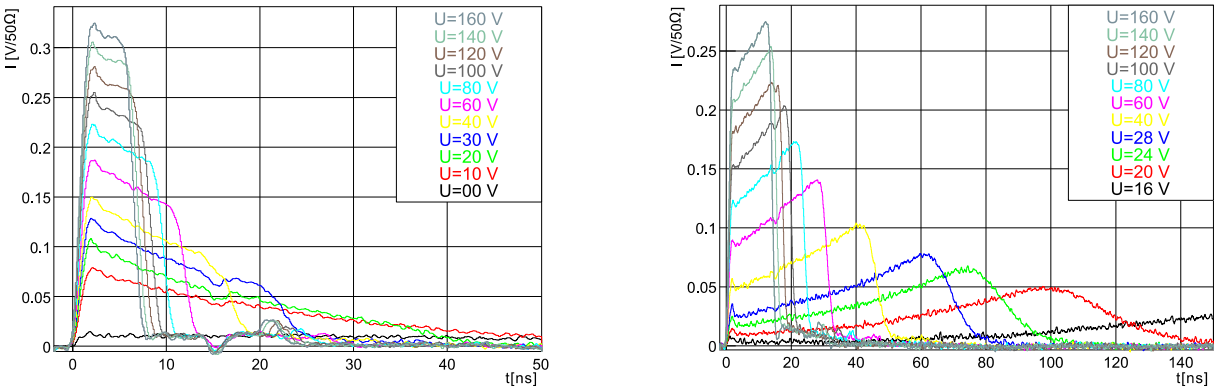

(a) (b)

Figure 5.3: Induced current pulses in a non-irradiated p-in-n silicon pad detector with $U_{\mathrm{FD}} = 14\,\mathrm{V}$ for (a) electron injection and (b) hole injection at different bias voltages; charge carriers were injected using a pulsed 670 nm laser [10].

contact of the electron injection ("front contact" in Fig. 5.2) and a lower electric field at the rear contact. Likewise, holes are injected at the opposite contact with the signal exhibiting the characteristic behaviour for an increasing electric field towards the front contact. These conclusions are in agreement with a positive effective space charge in the detector bulk, as expected for n-type silicon bulk, yielding an approximately linearly increasing electric field towards the p-type implant in the material. The exponential decrease during the pulse has already been derived in Eq. 5.18, with a second term additionally accounting for the decrease due to the finite lifetime of the charge carriers, which cannot be observed in this case since the lifetime is much longer than the transit time.

For a reverse bias smaller than the necessary voltage for full depletion U_{FD}, the electrons exhibit a reduced velocity whilst traversing the material towards the low field region. The result can be seen in Fig. 5.3 as well, causing a long tail in the signal. On the other hand, holes have to reach the depletion zone by diffusion, hence a relatively slow process, through the undepleted region before being swept by the electric field at late times. Accordingly, the described behaviour is inverted for negative effective space charge in the detector.

5.3 Development of the experimental setup

In order to study the current pulses and determine important figures of merit such as the CCD for different sensor materials, especially pCVD diamond, a Transient Current Technique setup was developed during the course of this work. As mentioned before, the required injection of charge carriers in the vicinity of an electrode can be done by either

a pulsed laser or α particles. In the case of silicon diodes red laser light has sufficient energy for the indirect band gap of silicon, whereas diamond samples require either a UV laser or α's. Therefore, a separate setup has been built for both of these sources. The setups were designed to be versatile and fulfil the following requirements:

- charge injection on both sides
- high bandwidth of the readout circuit in order to sample fast transients correctly
- shielding against ambient light and radio frequency (RF) noise
- sensors easily exchangeable
- readout circuit usable for both setups
- stable environment regarding temperature and humidity

The basic principles of the devised setups are illustrated in Fig. 5.4. The core components consist of the charge injection sources (laser or ^{241}Am α's), the DUT and an amplifier in a – preferably shielded – read-out circuit, the applied high-voltage bias, the waveform recording via oscilloscope and a PC for the purpose of storing the recorded waveforms and controlling the bias.

5.3.1 Pulsed laser setup

A pulsed red laser as charge injection for the TCT setup (in the following referred to as the *laser setup*) can be used to characterise materials with a sufficiently small band gap, such as silicon. Furthermore, this setup was developed with the intention to, firstly, verify the functionality of the setup and, secondly, implement the different data acquisition and analysis methods used to characterise sensor materials.

The laser diode itself is a *Picosecond Injection Laser* (PiLas) from Advanced Laser Diode Systems and has a wavelength of $\lambda = 671$ nm. The repetition rate of the laser pulses can be set in 1, 2 and 5 steps per decade for values between 100 Hz and 1 MHz or triggered externally. The light is coupled into a singlemode fibre which is subsequently connected to an attenuator and a microscope on top of a *Süss MicroTec PA 300* probe station. The TCT setup with the DUT is placed inside the probe station, which provides additional shielding against ambient light and RF noise. An optical cube inside the microscope is used to divide the beam, one half of which is then used to measure the laser intensity with a photodiode, whereas the other half is focused onto the sample. The

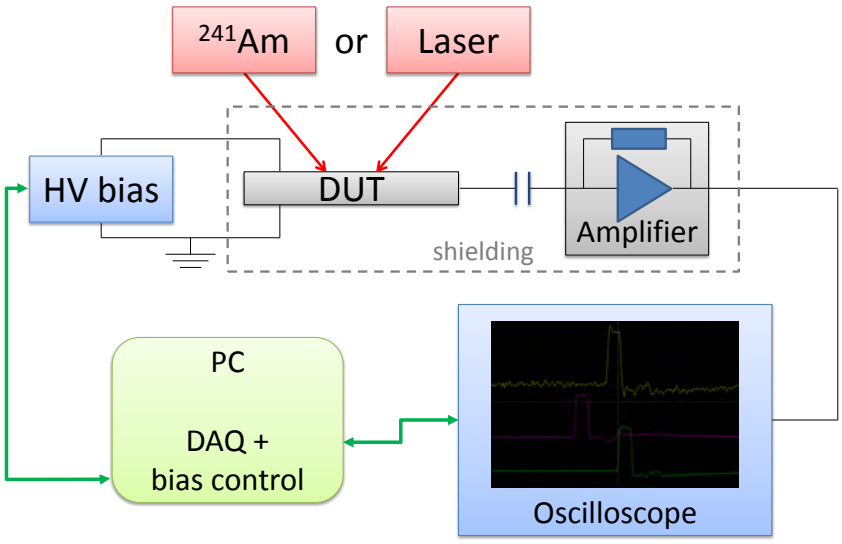

Figure 5.4: Illustration of the core components and principles of the TCT setups. Either a laser or α's from ^{241}Am decay are employed for charge injection. The signal is capacitively coupled into an amplifier and read-out via oscilloscope. Data acquisition (DAQ) and bias control are done via PC.

position of the beam spot can be checked via a camera. The whole laser beam path is shown in Fig. 5.5.

Given the absorption coefficient of silicon as $\alpha_{abs}(293\,\mathrm{K}) = 3.3\,\mu\mathrm{m}$ [10], electron-hole pairs are generated at a depth which is less than 2 % of the diode thickness $D = 250\,\mu\mathrm{m}$. Hence the contribution of carriers drifting to the adjacent electrode is negligible.

However, it has to be noted that the laser diode, attenuator, and photodiode are not very stable, especially regarding factors like temperature. Hence, in order to conduct precise measurements depending on the knowledge of the exact energy deposition in the DUT, it is required to calibrate the photodiode using a well-known *Front-End I3* module. The calibration procedure is extensively described in [33].

5.3.2 Americium-241 α source

^{241}Am decays 100 % by alpha transitions to ^{237}Np. Most decay products (84.6 %) populate the excited level of ^{237}Np with an energy of 59.54 keV, resulting in α emission exhibiting a kinetic energy of 5485.56 keV [34]. The activity of the employed source was determined in 2011 yielding 53 kBq. Taking into account the half-life of 432.2 years this activity supposedly has not diminished significantly since then.

The isotope itself is placed inside a steel vessel with the circuit board mounted in front

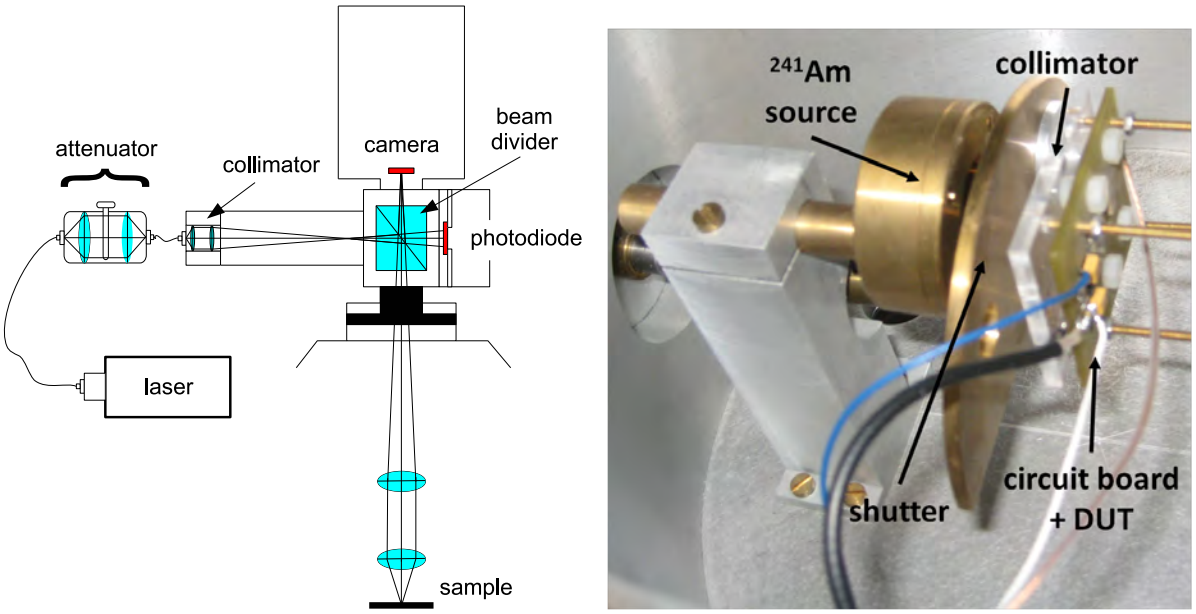

(a) (b)

Figure 5.5: (a): Schematic layout of the laser beam path in the microscope of the probe station. (b): Picture of the layout used in conjunction with the ^{241}Am source.

of it as shown in Fig. 5.5. The vessel can not only be evacuated, thus α's can cross the distance between source and DUT without being scattered off air molecules, but it also provides shielding against ambient light and RF noise. Apart from illuminating the target, the source can be blocked by a shutter or additionally attenuated by a $\approx 10\,\mu$m aluminium foil. The distance between source and DUT is ≈ 2 cm. A 5 mm thick acrylic glass collimator with a square opening of $5 \times 5\,\text{mm}^2$ is placed in front of the DUT in order to shield the conductors and components of the circuit from the ionising particles. As a result, the rate at which α's reach the sensor is ≈ 200 Hz, hence the probability of double pulses is negligible.

5.3.3 Data acquisition and analysis

TCT signals are readout by a Tektronix DSA 70804B oscilloscope with 8 GHz bandwidth and a sampling rate of 25 GS/s. The oscilloscope is connected via USB (GPIB) to a computer for the purpose of data acquisition. In order to control the oscilloscope and store recorded waveforms, a self-written acquisition programme has been devised. The programme was implemented by using *LabWindows* to create a graphical user interface (GUI), which is shown in Fig. 5.6. The user interface consists of three main parts: trigger adjustment, options for waveform recording, and remote control of the bias voltage supply.

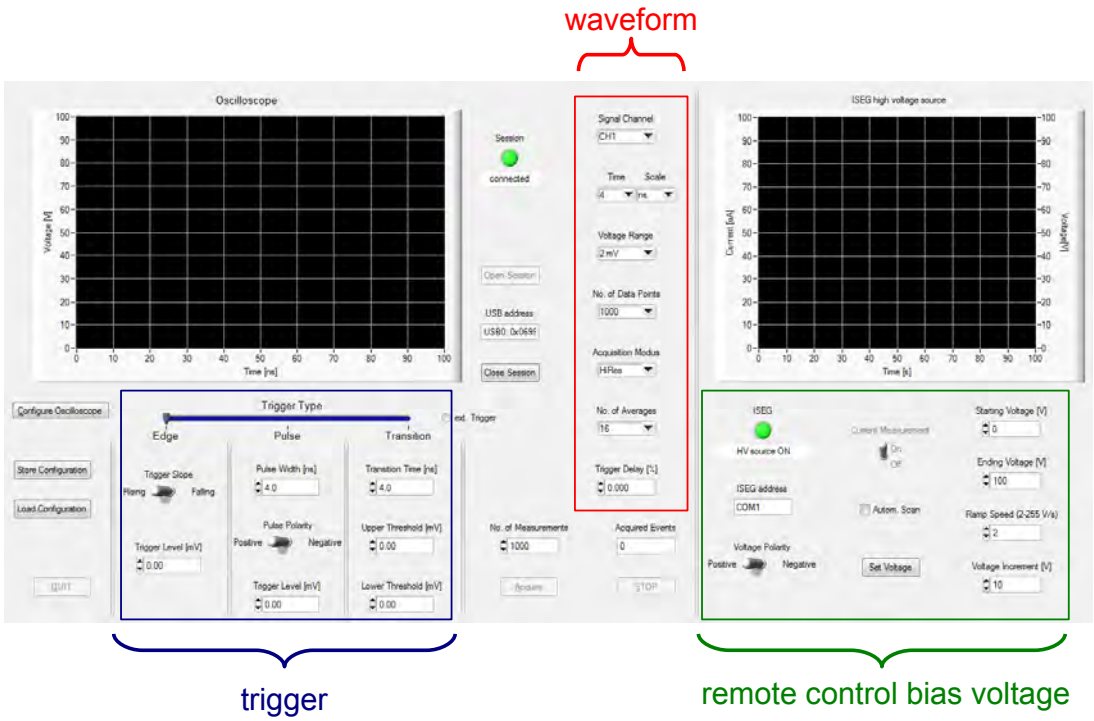

Figure 5.6: Graphical user interface developed for TCT data acquisition; three main parts of the interface are emphasised: trigger adjustment, waveform options, and bias remote control.

The adjustments of trigger and data acquisition with the programme correspond to the respective options available at the instrument itself. Moreover, the current adjustments in the oscilloscope can be adopted directly by the programme. The programme records and stores every waveform taken during data acquisition as a single ASCII file, which can be analysed offline. One scan consists of several recorded single waveforms, the number of which is selected beforehand in the programme. In addition, the scan can be aborted manually at any time. The configurations of the oscilloscope during data acquisition are saved as well and can be recalled for later measurements.

The control of the bias voltage is implemented such that the measurement can be conducted automatically in a selected voltage range. For this purpose, the bias voltage is increased by a selected increment after each completed scan, i.e. after the selected number of single waveforms have been recorded for the respective bias. During automatic scans, the current output of the bias voltage supply is recorded in conjunction with the voltage at the beginning of each scan, resulting in an I-V curve for the sample in addition to the TCT measurements. Another option is a scan at fixed bias, with the current measured for each single waveform.

The main principles of data analysis are the same for both TCT setups, however,

small deviations arise from the use of an external trigger in the laser setup in contrast to the Am setup. The ASCII files with the recorded data from the single waveforms are read individually by the analysis script and the voltage is averaged for each time bin of the oscilloscope, thus an average waveform is acquired for each respective bias voltage. Afterwards the average waveform is corrected for DC offset. In the case of the laser setup, an additional scan is performed without bias voltage in order to account for crosstalk between external trigger and signal line as well as to correct the pick-up of unwanted oscillations in the signal cable. However, before any single waveform of a measurement is analysed, every waveform is checked for repeated consecutive records of the same trigger and unaccounted pick-up of ambient noise during the signal pulses. This is especially important for the Am setup, for which the period between accepted triggers can be in the order of seconds.

5.3.4 Read-out circuit

The design of the read-out circuit is the crucial part in developing a TCT setup. The whole circuit has to operate under conditions including high-frequency components with a frequency $\mathcal{O}(100\,\mathrm{MHz})$ in the TCT pulses as well as support high-voltage DC bias. Analysing the setup for possible sources of unwanted effects and subsequently optimising the circuit has been the main work done during the course of this thesis, with the results presented in the following chapters.

The electric circuit used in the final layout for both TCT setups is shown in Fig. 5.7.

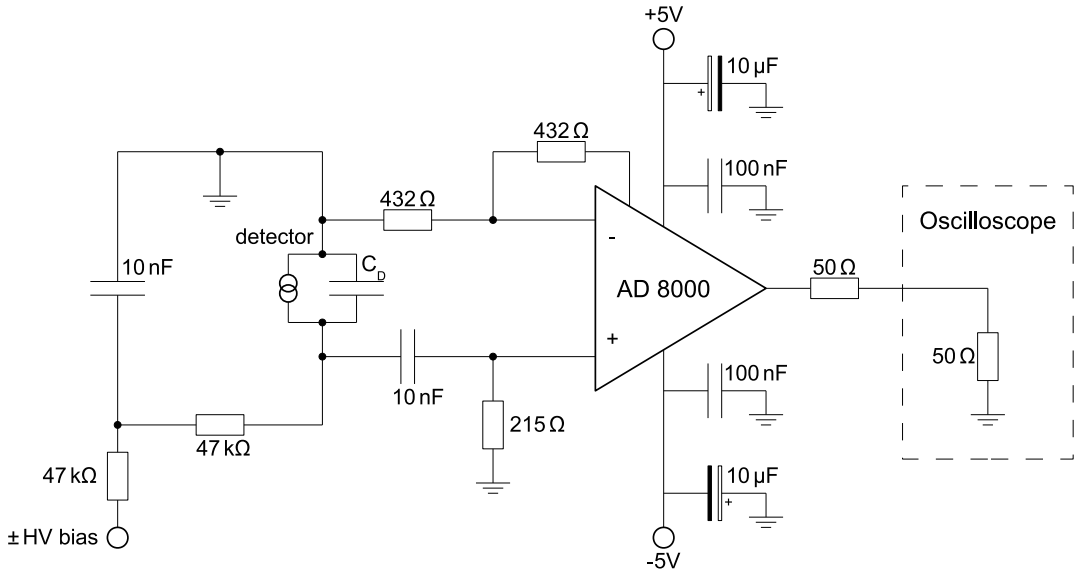

Figure 5.7: Setup used for the amplification and readout of TCT signals.

The circuit itself is composed around an operational amplifier *AD8000* (*Analogue Devices*), which is used for its wide bandwidth of 600 MHz and high slew rate of 3700 V/μs for small signals [35]. The amplifier is operated as a transimpedance amplifier with a 215 Ω input resistor in a non-inverting configuration due to board processing reasons and has a gain of $A = 2$. However, because of the output resistor, only half of the signal is measured in the oscilloscope, resulting in an overall unity-gain. Power supply bypassing for the amplifier is provided by one ceramic and one unipolar electrolytic capacitor for each supply input respectively. The whole circuit has been lain out on a *printed circuit board* (PCB), a picture of which is shown in Fig. 5.8. The layout was chosen due to its compact size and thus small stray inductance and capacitance.

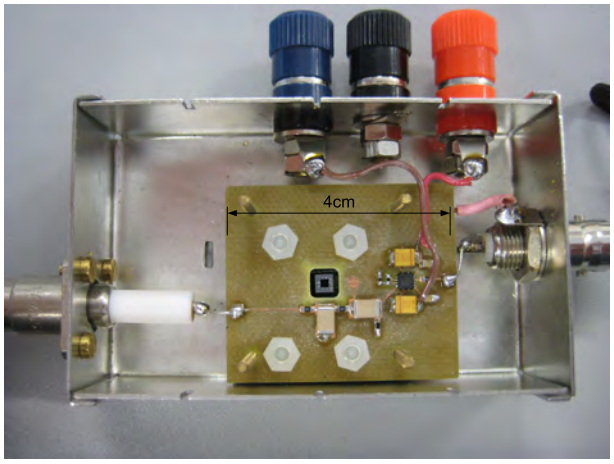

Figure 5.8: Circuit for TCT measurements lain out on a PCB and placed inside a metal box for shielding. This setup is used in conjunction with the pulsed laser diode.

An important observation at an early stage of setup development is the fact that RF noise – originating from the trigger output of the laser controller as well as from the cables connecting aforementioned controller to the laser diode – can couple into the setup. This observation is indicated in Fig. 5.9(a) with the measured voltage for DUT irradiation and blocked laser displayed. Further tests yielded that the oscillations before the signal pulse originate from the laser trigger, the ones after is a result from the coupling of the laser controller into the supply of the amplifier. The latter effect can be minimised by ensuring sufficient spatial distance between supply voltage and laser controller, the former can be taken into account by taking a reference measurement at 0 V bias and subsequently correcting the recorded waveforms.

Before the AD8000, a *VV1000-LC3E* preamplifier fabricated by *Kolter Electronic* has been used in the setups, measured TCT signals are shown in Fig. 5.9(b,c). However, that

amplifier was a separate component and could not be included on the board. This is especially problematic for the Am setup, where the amplifier had to be placed outside the vacuum vessel, separated from the circuit by an additional feed-through. Even though the overall gain of the amplifier, $(20.56 \pm 0.02)\,\mathrm{dB}$ (see section 7.1.2) over a $50\,\Omega$ resistor, was larger than in the current setup, additional oscillations during and after the signal peak can be seen. These are most likely due to reflections because of impedance mismatching at the amplifier input or output. Therefore an integrated circuit (IC) operational amplifier is used in the final setup. Additionally, the $50\,\Omega$ series resistor at the amplifier output is used in conjunction with the input impedance of the oscilloscope of the same magnitude to ensure that no oscillations occur, although the signal is halved.

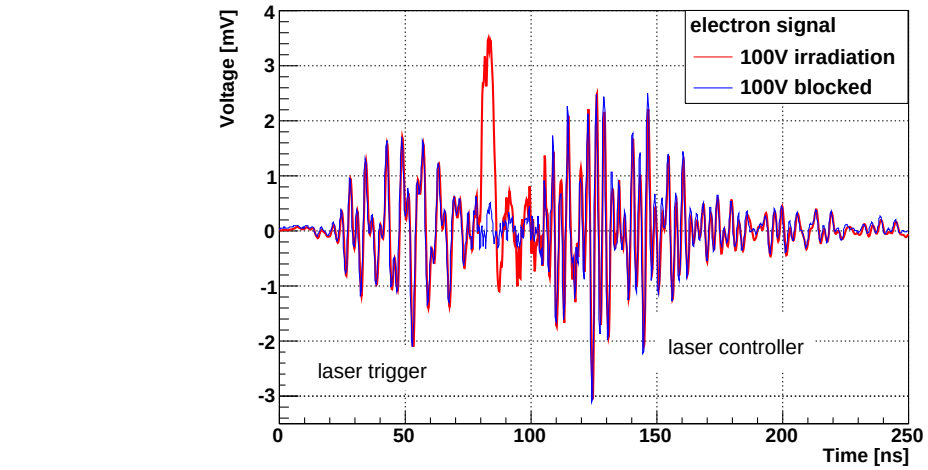

(a)

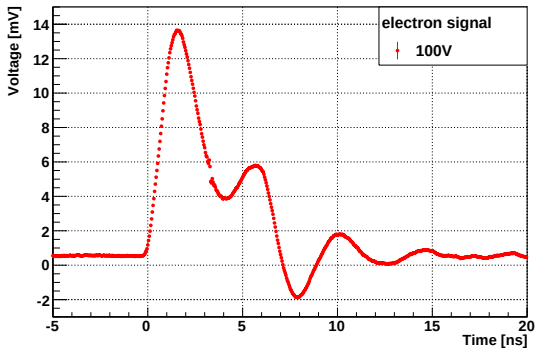

(b)

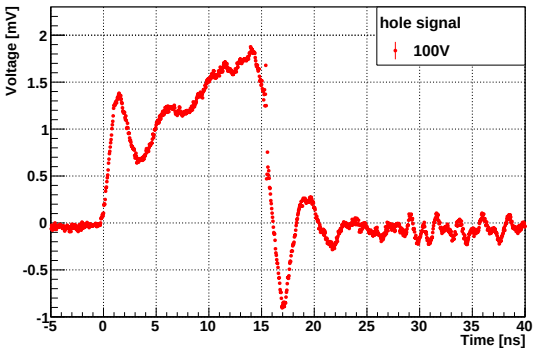

(c)

Figure 5.9: (a): TCT measurement with DUT irradiation (red) and blocked laser (blue) at bias $U = 100\,\mathrm{V}$. The sources of oscillations before and after the signal are noted. (b)/(c): TCT signals of electrons and holes respectively as measured with the old amplifier in a previous setup layout.

6 TCT measurements on a silicon diode

Before the characterisation of new sensor materials, such as diamond, can be done with the developed TCT setup, the measurement setups have to be verified by the usage of a well known sample. Therefore, extensive testing has been done with a silicon diode for both, the laser and the Am setup. The sample used is the same as described in section 4.2.1.

6.1 Determining the induced current pulse

The oscilloscope employed for the TCT setups measures signals in the form of voltage waveforms over a 50 Ω resistor. However, these signals are altered by various effects, such as the capacitance of the sensor and the bandwidth of the amplifier or oscilloscope. The latter two of these factors are negligible for the setup due to the high bandwidth of both, whereas the former must be taken into account.

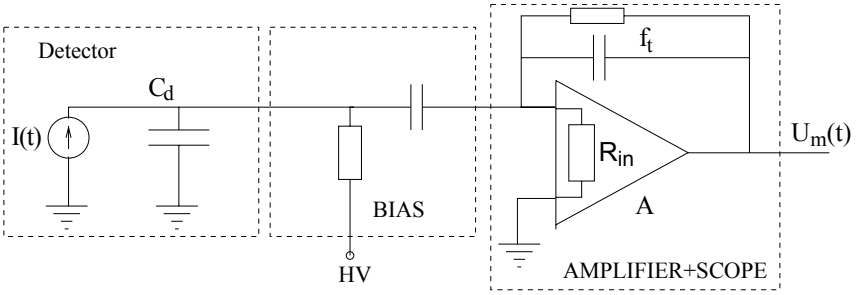

Figure 6.1: Equivalent circuit of the TCT setup used to extract the transfer function [10].

A circuit as shown in Fig. 5.7 acts as an amplifying low pass filter for which the transfer function ξ has to be calculated from the corresponding equivalent circuit, illustrated in Fig. 6.1, in order to yield the underlying induced current. The transfer function of the circuit in the frequency domain can be determined as follows assuming a constant amplification considering the large amplifier bandwidth [10]:

$$\begin{aligned} \frac{1}{Z} &= \frac{1}{R_{in}} + \mathrm{i}\omega C_d \qquad \text{, with} \quad \mathrm{i} = \sqrt{-1} \\ U_m &= AZI(\omega) = \xi(\omega) I(\omega) \\ \implies \xi(\omega) &= \frac{AR_{in}}{1 + \mathrm{i}\omega(C_d + C_s)R_{in}} = \frac{AR_{in}}{1 + \mathrm{i}\omega\tau} \end{aligned} \tag{6.1}$$

where U_m is the voltage as measured with the oscilloscope, I the induced current, C_d the detector and C_s additional parallel stray capacitances, and $R_{in} = 215\,\Omega$ the input impedance of the operational amplifier. Using the results of the C-V measurements for the capacitance of the diode with $C_d = 8.37$ pF, one finds a time constant $\tau \approx 1.8$ ns which corresponds to a cut-off frequency of $\nu_d = 88$ MHz. This is an order of magnitude lower than the bandwidth of the amplifier $\nu_\mathrm{amp} = 600$ MHz. Since the input capacitor has a relatively high capacitance of 10 nF, resulting in it being transparent for the induced current pulses due to the high bias and input resistor, it can be neglected in the calculation.

Determining the measured voltage in the time domain yields [10]

$$U_m(t) = \frac{AR_{in}}{\tau}\, \mathrm{e}^{-\frac{t}{\tau}} \int_{-\infty}^{t} I_m(t')\, \mathrm{e}^{\frac{t'}{\tau}}\ \mathrm{d}t' \tag{6.2}$$

The resulting underlying current pulse, as induced by the generated charges in the detector, is then calculated as follows [10, 36]:

$$I_m(t) = \frac{1}{AR_{in}} \left[R_{in}(C_d + C_s) \frac{\mathrm{d}U_m(t)}{\mathrm{d}t} + U_m(t) \right] \tag{6.3}$$

As mentioned before, recorded waveforms are averaged for each time bin of the oscilloscope and subsequently corrected for DC offset as well as trigger noise. The root mean square (RMS) of the respective mean value is used as the uncertainty on each averaged data point. In the case of the laser setup, the influence of the external trigger on the waveform can be easily corrected by conducting an additional scan with a bias of $U = 0$ V. This scan without an external field is averaged in analogy to all other measurements and subtracted from other averaged waveforms. The overall procedure with several single waveforms, their average waveform as well as the comparison between an uncorrected average waveform and the reference measurement without bias is displayed in Fig. 6.3.

The corrected average waveforms for electron and hole signals measured with the laser setup at different applied bias voltages are shown in Fig. 6.2. Although the general form of TCT pulses in n-type silicon is observable – including the decrease during the electron

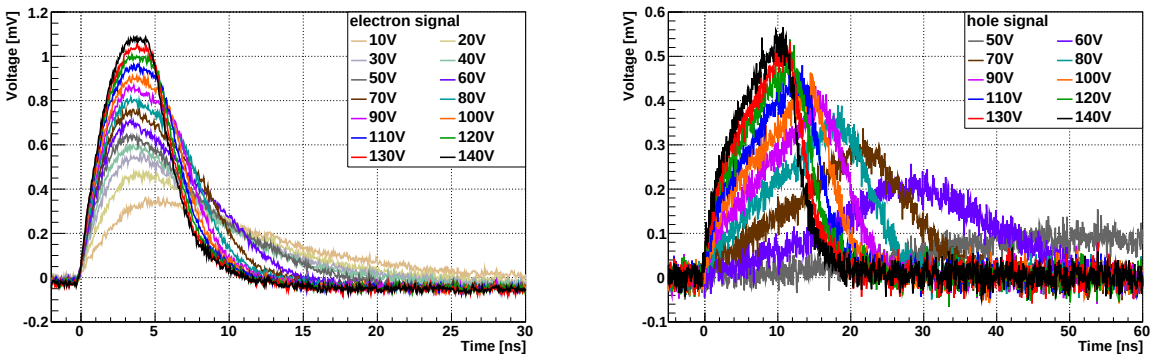

(a) (b)

Figure 6.2: Time-resolved voltage pulses in a silicon diode, averaged and corrected for trigger ringing: (a) electrons and (b) holes. The different scales for the time and voltage axes have to be noted.

signal and increase during the hole signal – relatively large fluctuations of the averaged voltage can be seen as well. These fluctuations are most likely due to the limited resolution of the voltmeter in the oscilloscope and, moreover, they lead to problems regarding the calculation of the derivative necessary to determine the current signal (Eq. 6.3).

Therefore an additional smoothing of the waveform has been employed before further TCT analyses are performed. The smoothing is done by making a linear fit for each data point, taking into account a number of preceding and following values. Evaluating the fit result yields the smoothed value for each data point with the respective 1σ confidence level as the uncertainty of the smoothed data. The smoothing procedure has been chosen such that the resulting waveform is more useful for further analyses, particularly with regard to calculating the derivative, while maintaining all signal features without loss of information, as shown in Fig. 6.4.

After the smoothing of the measured waveforms, the induced current pulses can be determined according to Eq. 6.3. For this purpose, $C = C_d + C_s$, i.e. the sum of detector and parallel stray capacitance, has to be derived. As it can be seen in Fig. 6.5(a) the right estimation of C is crucial in order to deconvolute the correct current pulse from the voltage curve. If C is estimated too large, the influence of the rising and falling edge is overestimated, leading to a bump during the pulse and an undershoot afterwards. If C is too small, the typical TCT signal features, e.g. the decrease/increase during the pulse, are less pronounced,which could even lead to an indication of the wrong effective space charge.

Another important aspect of signal deconvolution is the calculation of the derivative.

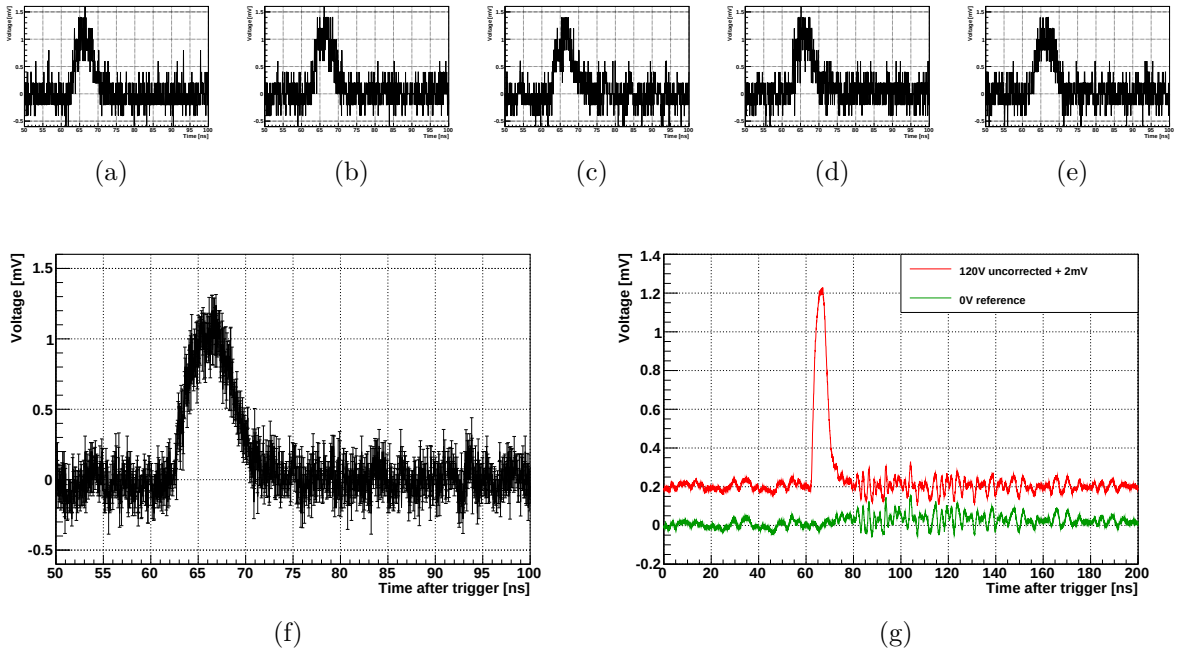

Figure 6.3: Recorded consecutive single waveforms for TCT measurement on the silicon diode at $U_{\text{bias}} = 120\,\text{V}$ (a)-(e), their averaged waveform (f), and the average waveform of all single measurements in comparison to the reference measurement conducted without bias (g). The apparent trigger ringing is subsequently corrected before further steps are done.

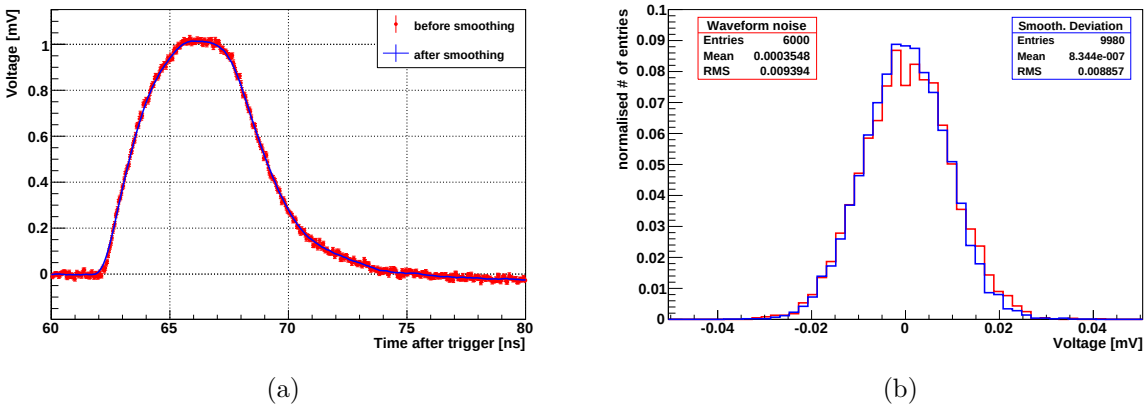

Figure 6.4: (a): Comparison of the measured waveform for electron signals at $U_{\text{bias}} = 120\,\text{V}$ before and after smoothing. (b): Comparison between the voltage distribution until directly before the TCT pulse (red), i.e. the input noise, and the deviation of the smoothed data from the original (blue). The smoothing parameter was chosen such that the RMS values are in the same order of magnitude. Similarly, it was ensured that no information is lost in the process for all measured waveforms.

This is done in analogy to the smoothing of the voltage curves by interpolating a number of data points before and after the respective point, in this case with a second-degree polynomial, for which the derivative is determined. As it can be seen in Fig.6.5(b), the exact number of data points used for this calculation also has an impact on the resulting current pulse. If an insufficient number of points is used, the pulse exhibits fluctuations due to the overestimation of small changes in the slope. An excess of points might suppress signal features, for instance by limiting the slew rate or signal height and hence leading to a systematic uncertainty for quantities such as transit time or collected charge.

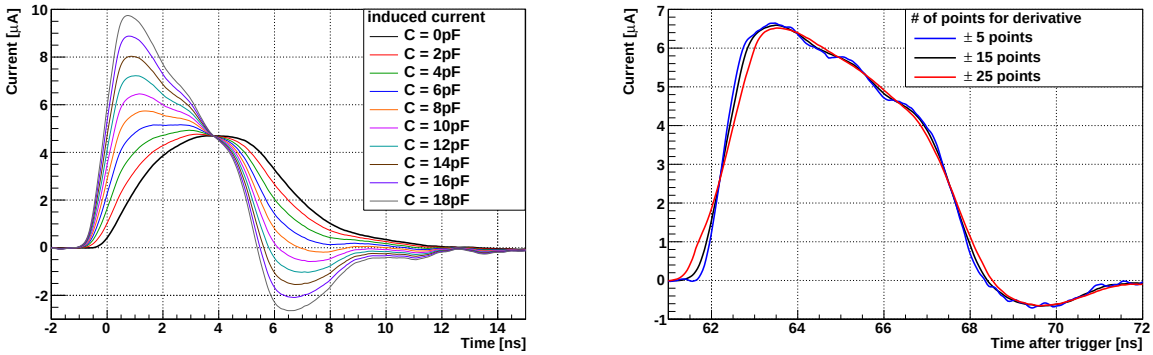

(a) (b)

Figure 6.5: (a): Measured current pulses for $U_{\text{bias}} = 120\,\text{V}$ deconvoluted with different values for C. (b): Current pulse for $U_{\text{bias}} = 120\,\text{V}$ deconvoluted with varying number of points taken into account for the calculation of the derivative. The derivative is calculated by interpolating a number of data points before and after the respective value.

The estimation of C is done by fitting the rising edge of the waveform for electron signals before being smoothed. The utilised fit function is a convolution of charging curve – accounting for the underlying RC network as shown in Fig. 6.1 – and a Gaussian error function, which takes into account the structure of the laser pulse:

$$U_m(t) = U_0 \cdot \left(1 - \exp\left(-\frac{t - t_\text{s}}{R_{in}C}\right)\right) * \frac{1}{2}\left(1 + \text{erf}\left(\mu_\text{laser}, \sigma_\text{laser}\right)\right) \tag{6.4}$$

Here, U_0 is the parameter which accounts for the signal height, t_s the beginning of the capacitor charging, $R_{in} = 215\,\Omega$ the amplifier input resistor, μ_laser the sampling instance of the laser pulse, and $\sigma_\text{laser} \leq 14.5\,\text{ps}$ the pulse width with an upper boundary as specified in the manual of the laser diode [37]. The choice of this fit function not only provides a good description of the rising edge, which can be seen in Fig. 6.5(b), but also yields

fit results with reasonable χ^2/ndf between 0.65 and 1.45. The results of the fit for the parameter C is shown in Fig. 6.6. It can be seen that the resulting C-V sweep exhibits a behaviour similar to the previously described C-V measurements (Fig. 4.6). Additionally, the capacitance of the diode at full depletion can be determined by fitting a constant to the values for bias $> U_{\mathrm{FD}}$ resulting in $C_{\mathrm{FD}} = (10.3 \pm 0.2)$ pF. From the result for C_{FD} the effect of stray capacitance C_s on C can be estimated yielding $C_s = 2$ pF. In order to deconvolute the measured voltage curves, this value for C_s is used in conjunction with the results of the C-V sweep (section 4.3.2), since the dedicated C-V measurement is more precise than the fit result.

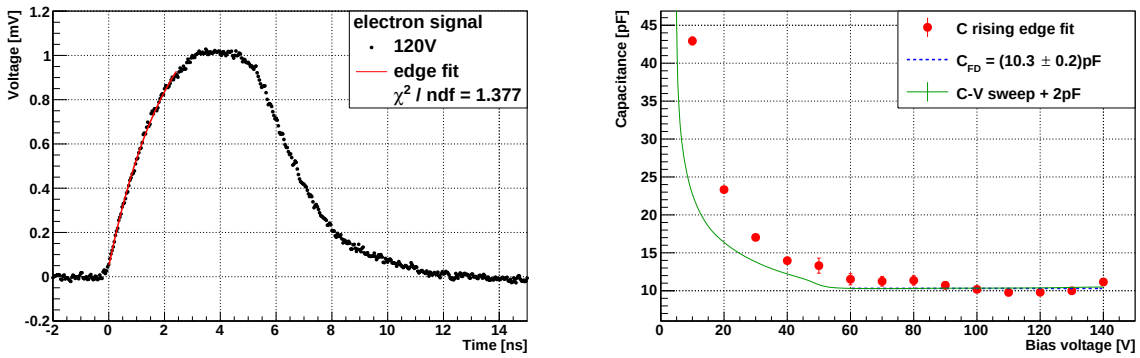

(a) (b)

Figure 6.6: (a): Fit of the rising edge of a TCT pulse used to determine C. (b): Parameter C vs. bias voltage as results from the fit of the rising edge. For bias $> U_{\mathrm{FD}}$ a constant is fitted to the values of C with the result displayed.

Estimation of uncertainties

During the process of averaging, smoothing and deconvolution the waveforms, statistical as well as systematic uncertainties arise from the respective procedures. The statistical uncertainties are included and propagated for all steps of signal processing as follows: since smoothing and deconvolution both include polynomial fits to a number of data points, the statistical uncertainties are directly derived from the fit results. In the case of smoothing, where the fit is evaluated at a specific point yielding the smoothed data point, the 1σ confidence interval of this evaluation is used as the statistical uncertainty of the resulting smoothed data. For deconvolution, in which case the derivative is determined from a fitted second-degree polynomial, the used ROOT classes offer the direct estimation of error of the derivative. This is done by varying the fit parameters of the function within their respective uncertainties.

The exact estimation of all systematic uncertainties introduced by the used processes is a task going beyond the scope of this thesis, the main task of which was the development of the TCT setup. However, an estimation of systematics can be done by varying the processes to a certain extent, some of which have already been discussed in the previous section. The choice of the number of points included in the smoothing procedure is one main source of systematic uncertainty. Therefore it was ensured that the deviation of the smoothed data from the original do not deviate by more than the margin of noise in the original data, as shown in Fig. 6.4(b), and thus that signal features like the pulse height are not altered. Hence the magnitude of this systematic has been estimated $< 0.5\,\%$ for the integral of the pulse with respect to the original waveform and $\sim 1\,\%$ for the pulse length. Lastly, the number of data points used in the derivative have a strong influence on the structure of the resulting current pulse, especially the pulse length. One can find that varying this parameter leads to a relative uncertainty of about $5\,\%$ on aforementioned length, whereas the pulse integral is only altered by $\sim 1\,\%$.

6.2 Laser setup

Using the previously described methods to determine the induced current pulses in TCT measurements yields the results shown in Fig. 6.7. The key features of TCT signals are observable in the curves for both charge carrier. The different scaling of the x- (time) and y-axis has to be noted while interpreting the results. As expected due to their smaller mobility, hole signals provide a pulse width that is a factor of $2 \ldots 3$ larger than the respective electron signal, with the signal height being reduced by the same factor. Moreover, the decrease during the electron pulse and the increase during the hole pulse clearly indicate the positive effective space charge of n-type silicon bulk material.

In order to calculate the CCD, the mobility and lifetime of electrons and holes have to be derived from the current pulse, which is described by Eq. 5.18:

$$I_{m_{e,h}}(t) \propto \exp\left(\frac{\mp z t}{\tau_{\mathrm{eff}_{e,h}}} - \frac{t}{\tau_{e,h}}\right) \tag{6.5}$$

with z being the sign of the effective space charge in the detector bulk, and $\tau_{e,h}$ denoting the charge carrier lifetime. $\tau_{\mathrm{eff}_{e,h}}$ is the transient time constant given by [10]:

$$\tau_{\mathrm{eff}_{e,h}} = \frac{\varepsilon\varepsilon_0}{e\mu_{e,h}\,|N_{\mathrm{eff}}|} = \frac{\varepsilon\varepsilon_0 U}{e\overline{v_{D_{e,h}}} D\,|N_{\mathrm{eff}}|} \approx \frac{\varepsilon\varepsilon_0 U t_c}{eD^2\,|N_{\mathrm{eff}}|} \tag{6.6}$$

due to the behaviour of the electric field in the sensor.

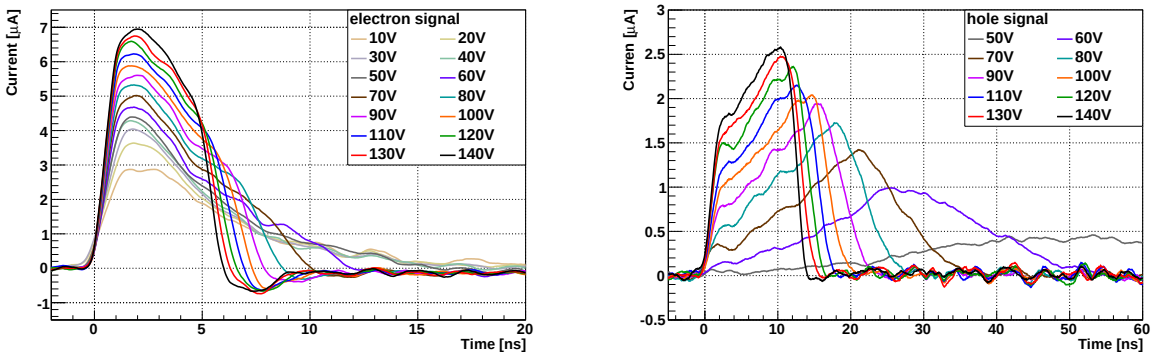

(a) (b)

Figure 6.7: Measured current pulses for different bias voltages after deconvolution: (a) electron and (b) hole signals.

6.2.1 Determination of charge carrier mobility

Determining the charge cloud drift time t_c from the rising and falling edges provides a direct measurement of the average drift velocity v_D with

$$v_D(E) = \frac{D}{t_c} \tag{6.7}$$

where D is the drift length of the drift which coincides with the detector thickness due to the charge injection in the vicinity of one electrode. The transit time $t_c = t_e - t_s$ itself is defined as the time between 10 % of the amplitude during the rising edge and the arrival of the centre of mass of the charge cloud at 50 % amplitude on the falling edge in the respective current pulse. To derive these points, the rising and falling edge of the signal is fitted with an error function and a complementary error function respectively (see Fig. 6.12) from which t_s and t_e are derived as fit parameters with the corresponding statistical uncertainties. An additional uncertainty on the transit time is introduced by the deconvolution procedure. This systematic uncertainty is estimated by varying the number of data points used to calculate the derivative and as a result accounts for $\delta t_c = 5\,\%$ of the determined transit time t_c.

Since the applied detector voltage can be quite high and the electric field is not constant due to space charges, the linear relation between drift velocity and electric field strength is no longer valid (in analogy to Eq. 5.17). In order to account for a reduction of the mobility due to scattering off ionised dopants and hence deviations from the ohmic low-

field mobility $\mu^0_{e,h}$, the empirical formula is used [29, 36]

$$v_D(E) = \frac{\mu^0_{e,h} E}{1 + \left(\frac{\mu^0_{e,h} E}{v^{\text{sat}}_{e,h}}\right)} \tag{6.8}$$

with $v^{\text{sat}}_{e,h}$ being the saturation drift velocity of electrons and holes respectively.

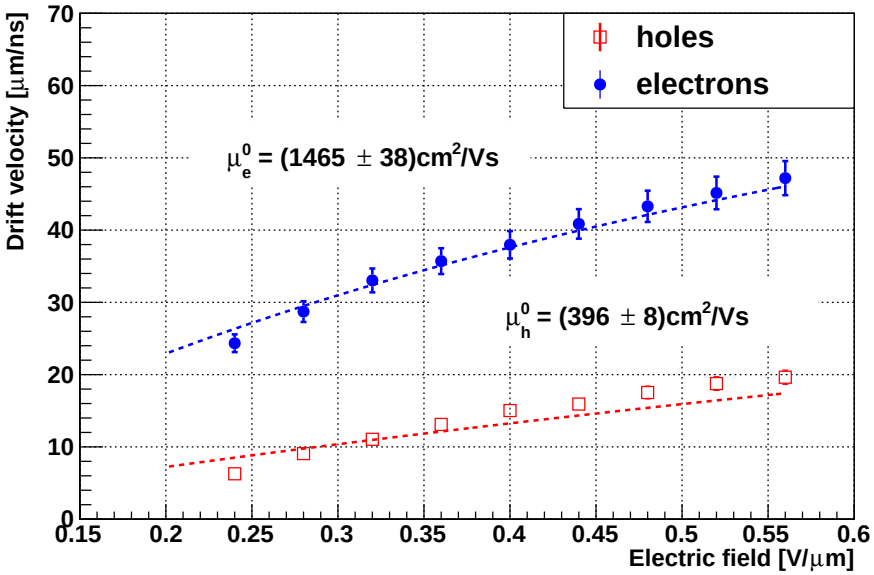

Figure 6.8: Average drift velocity determined from the TCT current pulses versus the applied electric field for both holes and electrons. Eq. 6.8 is fitted to the data points yielding the displayed mobility. Error bars for the hole data are mostly too small to be seen.

Eq. 6.8 is subsequently fitted to the plot of the drift velocity versus the applied electric field, shown in Fig. 6.8. Only current pulses with bias $U_{\text{bias}} \geq 60\,\text{V} > U_{\text{FD}}$ are included, as only for those the charge carrier transport occurs via drift across the whole detector length. The saturation velocity is limited by the respective values for room temperature with $v^{\text{sat}}_e(300\,\text{K}) \leq 105 \times 10^5\,\text{cm/s}$ and $v^{\text{sat}}_h(300\,\text{K}) \leq 81 \times 10^5\,\text{cm/s}$, respectively [38].

The result is a low-field electron mobility of $\mu^0_e = (1465 \pm 38)\ \text{cm}^2/\text{Vs}$, which is, within the margin of error, in good agreement with the known literature value of $\mu^0_e = 1450\,\text{cm}^2/\text{Vs}$ [18]. The fit yields a hole mobility of $\mu^0_h = (396 \pm 8)\ \text{cm}^2/\text{Vs}$, which deviates from the literature value $\mu^0_h = 440\ \text{cm}^2/\text{Vs}$ [18], however, μ^0_h is often inconsistent with regard to different publications.

In conclusion, it can be seen that the devised TCT setup is working well in conjunction with the laser, leading to results which are in agreement with known literature values.

The effective trapping time is not included in the results shown here because a well defined charge injection is important for this analysis and laser diode power exhibits too unstable and would require extensive and repeated calibration. All in all, the functionality of the TCT setup is verified using the laser source.

6.3 Am setup

In general, data acquisition and analysis for the Am setup is done in analogy to the laser setup as described in the previous sections. Though, since no external trigger is present in the setup, triggering is accomplished on the signal itself. However, the signal trigger introduces an artefact in the form of ringing at the instance of triggering, which has to be removed analogous to the smoothing procedure. Fig. 6.9(a) shows a waveform as measured with the oscilloscope, the respective smoothed waveform and the isolated trigger ringing.

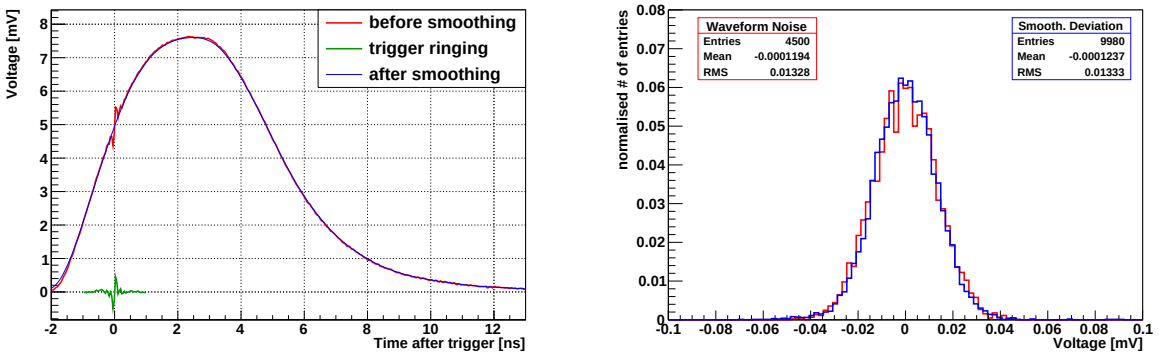

(a) (b)

Figure 6.9: (a): Comparison of the measured waveform for electron signals at $U_{\text{bias}} = 120$ V before (red) and after smoothing (blue). During the process of smoothing the observable trigger ringing (green) is removed as well. (b): Comparison between the voltage distribution until directly before the TCT pulse (red) and the deviation of the smoothed data from the original (blue). It can be seen that the RMS values are in the same order of magnitude.

As expected, the current signals measured with the Am setup (Fig. 6.10) exhibit a similar behaviour with respect to the corresponding measurements with the laser, albeit with a much larger signal height due to the high kinetic energy (5.486 MeV [34]) of the α particles of the ^{241}Am source. An additional feature which is observable in the electron signals, is the slightly delayed peak in comparison to the laser signals. A remarkable aspect of this signal feature is that the delay apparently increases with smaller bias. This

behaviour is most likely due to the so called *plasma effect*: due to the large number of electron-hole pairs injected with α particles, the generated charge cloud exhibits a high local field strength. Thus the separation of electrons and holes is delayed increasingly for a smaller applied external field.

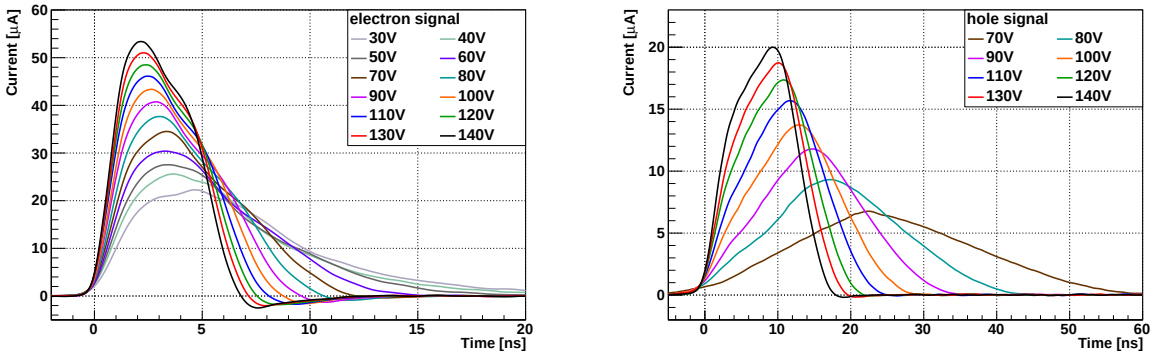

(a) (b)

Figure 6.10: Measured current pulses for different bias voltages after deconvolution: (a) electron and (b) hole signals.

The charge carrier mobility is determined in analogy to the laser setup by fitting Eq. 6.8 to the plot of the average drift velocity versus the applied electric field. The results are shown in Fig. 6.11. The fit for the electron data yields a low-field mobility of $\mu_e^0 = (1542 \pm 158)\,\mathrm{cm}^2/\mathrm{Vs}$. Within the margin of the rather large error – presumably because of an overestimated systematic uncertainty –, this value coincides with the same result derived from the results of the laser setup. Moreover, it is also in good agreement with the literature value $\mu_e^0 = 1450\,\mathrm{cm}^2/\mathrm{Vs}$ [18], whereas the hole mobility $\mu_h^0 = (345 \pm 8)\,\mathrm{cm}^2/\mathrm{Vs}$ deviates from both, literature value and previous result.

6.3.1 Determination of effective trapping time

Charge trapping during the drift leads to a reduced signal, provided the charge carrier lifetime $\tau_{e,h}$ is in the order of or smaller than the transit time t_c. The lifetime can be determined by several methods, the one which is used in the following utilises the integration of the measured current pulses in order to obtain the total injected charge. In addition, the applied voltage has to be sufficiently high above U_{FD} for this method, such that the effect of the space charge can be neglected, since according to Eq. 6.6 the corresponding time constant increases with higher voltage.

The *method of relative charge deficit* uses the relation of the charge carrier lifetime and the average drift velocity to the relative difference of the integrated measured current

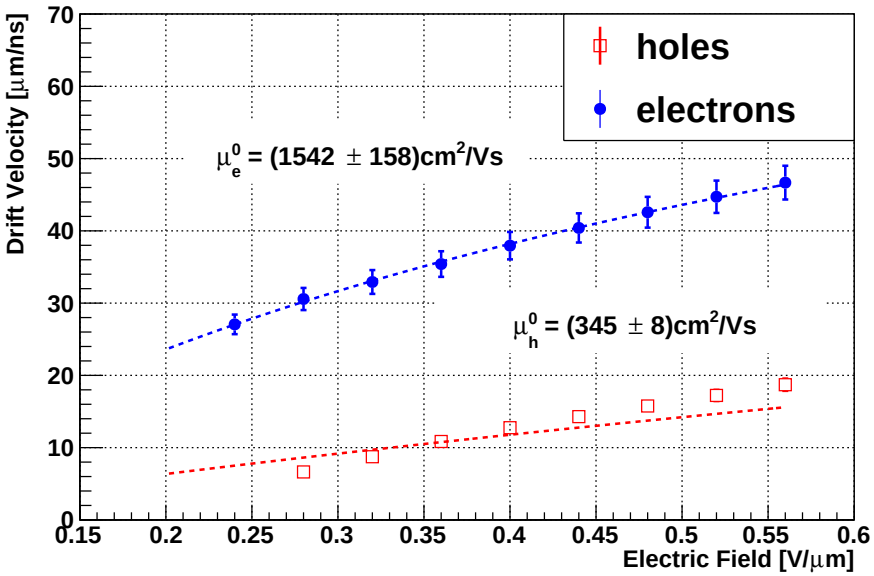

Figure 6.11: Average drift velocity determined from the TCT current pulses versus the applied electric field for both holes and electrons. Eq. 6.8 is fitted to the data points yielding the displayed mobility. Error bars for the hole data are mostly too small to be seen.

pulse $Q_{e,h}$ to the total generated charge $Q^0_{e,h}$ in the absence of trapping [10, 36]:

$$Q_{e,h} = \int_{t_s}^{t_e} I_{m_{e,h}}(t)\,\mathrm{d}t = \int_{t_s}^{t_e} I^0_{e,h}(t)\exp\left(-\frac{t-t_s}{\tau_{e,h}}\right) \approx Q^0_{e,h}\left(1-\frac{t_c}{2\tau_{e,h}}\right)$$
$$\Longrightarrow \quad \frac{Q^0_{e,h}-Q_{e,h}}{Q^0_{e,h}} \approx \frac{t_c}{2\tau_{e,h}} = \frac{D}{2\tau_{e,h}v_{D_{e,h}}} \tag{6.9}$$

$Q^0_{e,h}$ itself is determined by extrapolating Eq. 6.9 to infinite drift velocity, i.e. to $t_c = 0\,\mathrm{ns}$. The current pulses are integrated over the transit time $t_c = t_e - t_s$ as defined in the previous section, therefore any systematic errors which apply to the determination of the transit time also alters the charge measurement. Furthermore, in order to calculate the integral of the current pulse, not only the rising and falling edge are fitted the way it was done for the drift time, but also the pulse shape itself is fitted according to Eq. 6.5 (see Fig. 6.12). In order to account for systematic uncertainties introduced because of the fit, the deviation from the direct integral of the data is used as an additional relative uncertainty, which is generally in the order of $\sim 2-5\,\%$. Thus this uncertainty dominates with respect to the statistical uncertainty from the integral of the fitted pulse.

The collected charge as measured with the Am is shown in Fig. 6.13(a). It can be

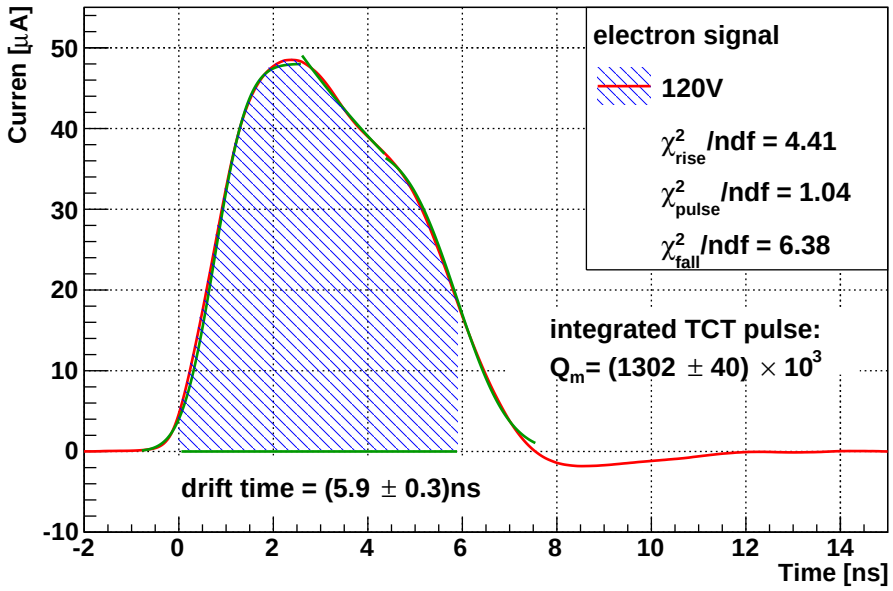

Figure 6.12: Measured current pulse for a bias voltage of 120 V with the edges and the pulse structure fitted. The resulting drift time and the integral of the pulse are shown as well with the corresponding values displayed.

seen that the collected charge progresses towards saturation at high bias voltage, albeit there is a difference between the measured charge of electron and hole signals for the same bias voltage. However, by plotting these values versus the transit time of the charge cloud and extrapolating towards $t_c = 0$ ns, one can see that the total number of generated charges agrees within the margin of error with $Q_e^0 = (1.46 \pm 0.04) \times 10^6$ e and $Q_h^0 = (1.42 \pm 0.04) \times 10^6$ e. Furthermore, using the mean value $Q_0 = (1.44 \pm 0.03) \times 10^6$ e and the kinetic energy of the Am α's to determine the average energy for electron-hole pair generation, one finds

$$E_{e-h} = \frac{E_\alpha}{Q_0} = (3.81 \pm 0.08)\,\text{eV} \tag{6.10}$$

which is in agreement with the known literature value $E_{e-h} = 3.6$ eV [18]. In order to minimise the effect of the transient time constant and considering the behaviour of the collected charge for increasing bias, only data points with an applied bias $U > 90$ V are included in the fit.

The same fit yields the effective trapping time of the charge carriers according to Eq. 6.9 with $\tau_e = (27 \pm 3)$ ns and $\tau_h = (48 \pm 3)$ ns. In combination with the determined charge

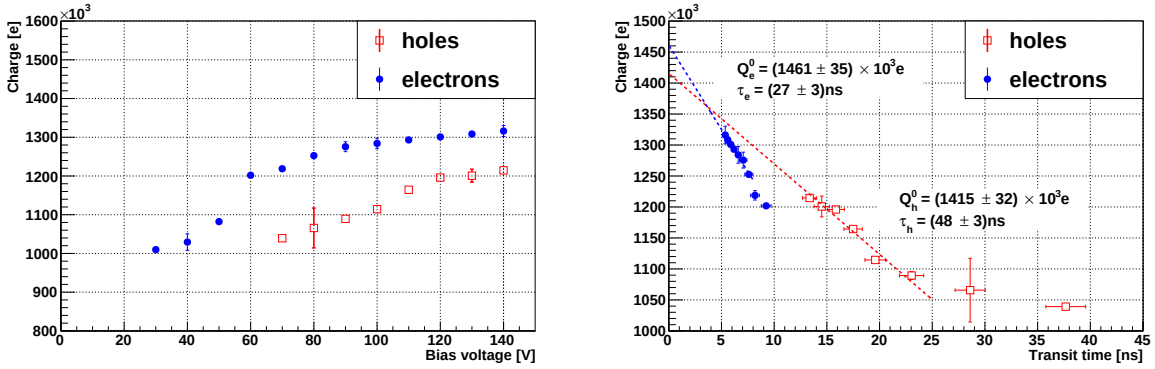

(a) (b)

Figure 6.13: (a): Total collected charge in the silicon diode, determined by integrating the respective TCT pulses, vs. the applied bias voltage. (b) Collected charge vs. the transit time of the respective charge cloud for electrons and holes. The charge deficit method (Eq. 6.9) is used to determine the displayed results for the total generated charge and carrier lifetime.

carrier mobilities and Eq. 3.1 one finds a CCD of the characterised device of

$$\mathrm{CCD} = (\mu_e \tau_e + \mu_h \tau_h)\, E = [(23 \pm 3) \cdot U]\ \mu\mathrm{m} \tag{6.11}$$

Given the diode thickness of 250 μm, this result is in good agreement with the observations during TCT measurements, since signals can already be measured at bias voltages as low as $U = 10\,\mathrm{V}$.

In conclusion, the α source provides an extended functionality with regard to the laser source due to the well defined charge injection using α particles. Moreover, the larger signals reduce the overall signal to noise ratio, thus allowing for a trigger on the signal itself. The results yielded by the setup is in good agreement with the corresponding results for the laser source. Additionally, the average energy for electron-hole pair generation and the effective trapping time has been determined, hence the CCD of the DUT can be derived resulting in a reasonable value, given previous observations. All in all, in a closure test the functionality of the TCT setup as well as the analyses methods have been verified.

7 TCT measurements on pCVD diamond

The transient current technique is applicable to CVD diamond detectors, however, due to the large band gap of diamond, charge injection has to be done by sources with rather high energy such as α particles. In this case the source of choice is a collimated ^{241}Am α source, since it provides ionising particles with an energy of 5.486 MeV [34], yielding $\sim$ 400,000 electron-hole pairs in the sample. Furthermore, α particles have a very short penetration depth of $\sim 14\,\mu$m [36], hence in comparison to the detector thickness, they are absorbed in a small range below the electrodes. However, care has to be taken regarding the source, in order to avoid polarization effects due to an accumulation of charges underneath the injection contact. Therefore an α source with a low activity at the DUT, like the employed ^{241}Am source, should be preferred.

7.1 Experimental setup

The experimental setup used to measure the pCVD diamond sample is nearly the same TCT setup as used for the ^{241}Am α source. However, there are two notable changes: the sample with its specifications – especially the detector capacitance – and the use of an additional amplifier. These changes are discussed in the following.

7.1.1 pCVD diamond sample

The sample *DB-DS-59* is an old pCVD diamond sample, shown in Fig. 7.1. The diamond has lost its optical quality and features a significant opaqueness, which is an indication that the sample was exposed to high fluences of irradiation. Moreover, the diamond provides an overall smaller grain size than newer samples, hence more grain boundaries are present, which further enhance the trapping probability. Since the seed and growth side are clearly distinguishable, the diamond was not polished after fabrication.

The diamond surface is quadratic and has an area of approximately $1 \times 1\,\text{cm}^2$. The

thickness of the diamond is (400 ± 10) μm. The circular electrodes have a diameter of (6.079 ± 0.001)mm [39]. This diamond sample has already been characterised in a previous work [39], yielding a capacitance of $C_d = (3.94 \pm 0.03)$ pF among others. In analogy to the silicon diode discussed in the previous section, this capacitance is used in conjunction with the stray capacitance $C_s = 2$ pF of the setup in order to deconvolute the measured TCT waveforms.

(a) (b)

Figure 7.1: Pictures of the pCVD diamond sample used for TCT measurements: (a) growth side and (b) substrate side.

7.1.2 Determination of amplification

Because of the optical and electrical shortcomings of the diamond sample, the signal height was expected to be too small for sufficiently efficient triggering. Therefore the VV1000-LC3E preamplifier was used in addition to the setup applied to silicon diodes. The amplifier was placed outside the vacuum vessel after the feed-throughs, thus it provides the additional amplification after the operational amplifier on the board. Due to the careful impedance matching at the output of the operational amplifier, the previously observable oscillations (see section 5.3.4) could be eliminated.

The core component of the preamplifier is a field-effect transistor whose gain was denoted with (22 ± 1.5) dB in the data sheet [40]. Since the uncertainty is too large for precision measurements, the amplification had to be determined more precisely under the conditions of TCT measurements. For this reason, a frequency generator was used to provide unipolar pulses with a rise time of 0.8 ns, a pulse length of 5 ns and a repetition rate of 100 Hz. The amplitude was varied thus yielding the amplification as the result of a linear fit to the plot of input vs. output amplitude, as shown in Fig. 7.2.

The result for the gain is $A = (20.56 \pm 0.02)$dB. Since a total of 128 single measurements were averaged for each data point, the resulting statistical uncertainty is quite small with $< 0.1\,\%$, hence it can be neglected for further analyses.

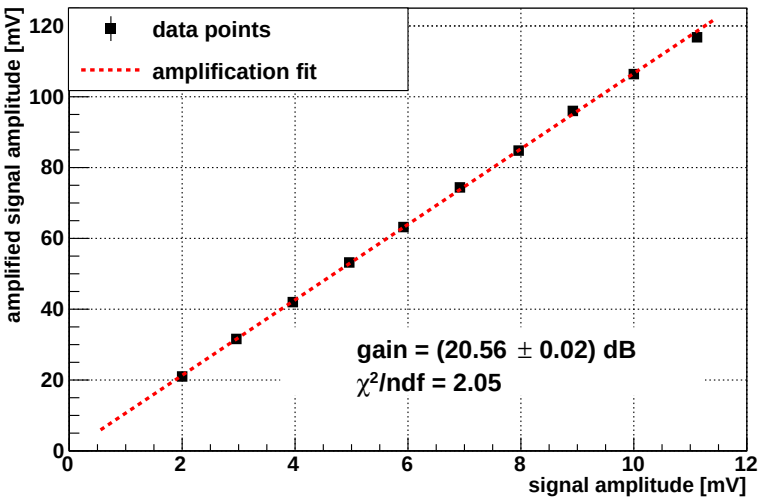

Figure 7.2: Amplitude of test pulses at the preamplifier output vs. input amplitude, respective error bars are too small to be seen. Amplification is determined by a linear fit, the uncertainty on the gain is the uncertainty of the fit result.

7.2 Results

Measurement results conducted with the diamond sample are processed and analysed in analogy to the signals for silicon. The obtained current pulses are shown in Fig. 7.3.

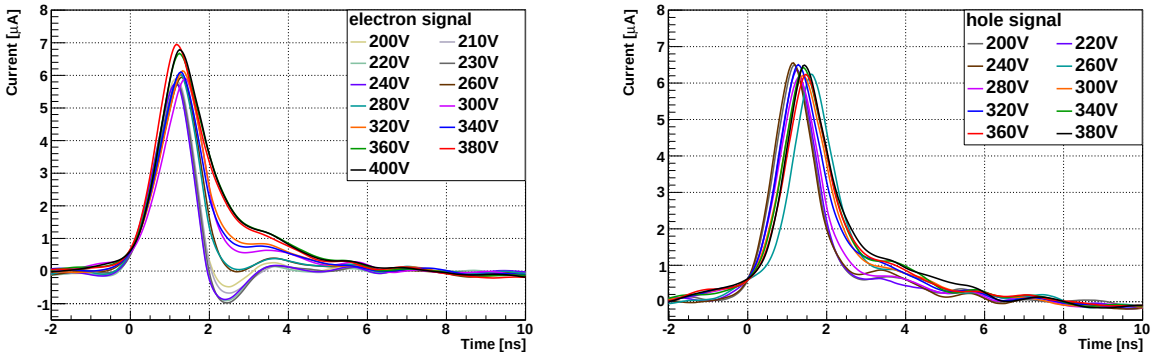

(a) (b)

Figure 7.3: Measured current pulses for different bias voltages after deconvolution: (a) electron and (b) hole signals.

Regarding the interpretation of this results, one has to note that the CCD of the sample is much smaller than its thickness [39]. Therefore the majority of charge carriers are trapped before reaching the electrode, yielding a steep exponential decrease after the signal peak. The resulting current pulses do not exhibit the behaviour seen previously for

silicon, the pulse structure of which was dominated by the influence of the effective space charge. Additionally, the drift time is in the same order of magnitude for both electrons and holes.

Another feature of the signals is the apparent difference between the pulse shapes of electron signals with a small bias in comparison to those with a larger bias and all of the hole signals. As the electron signals have been measured before the hole signals – ramping the voltage from the lowest to the highest value – and between measurements the diamond was shielded against ambient light, a possible explanation for the difference, is the pumping of defects in the sample and the arising polarisation field. The influence of these effects on the collected charge and the CCD has already been investigated in [39].

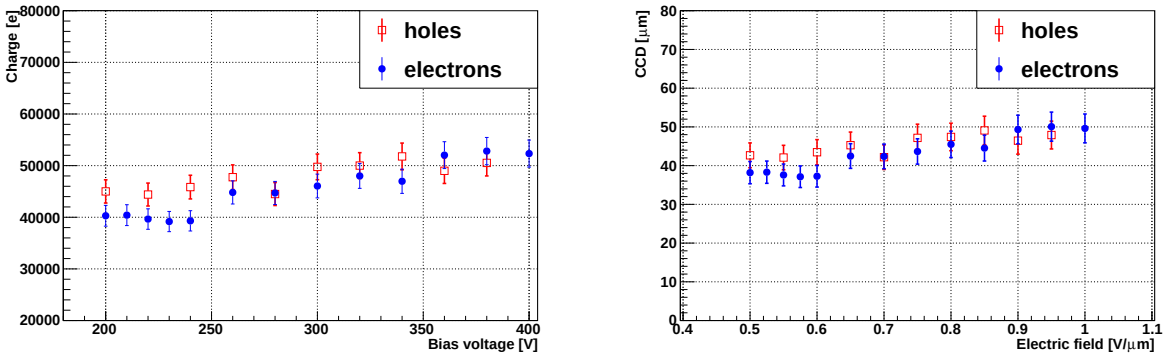

(a) (b)

Figure 7.4: (a): Total collected charge in the diamond vs. the applied bias voltage. (b) CCD of the diamond according Eq. 3.2 versus the applied electric field.

Since the detector thickness D exceeds the CCD ($D \gg$ CCD), the CCD can be determined from the collected charge by Eq. 3.2. The plots for the collected charge versus the bias voltage and the resulting CCD versus the electric field are shown in Fig. 7.4. The relative uncertainty on the CCD is slightly larger than for the charge because of the uncertainty on the sample thickness. The order of magnitude of the CCD is in the same region as determined before ([39]), however, the exact values differ.

8 Summary and Outlook

Diamond not only represents one of the most promising substances regarding radiation hard pixel detectors, but also offers many challenges. Although diamond synthesis using chemical vapour deposition is able to provide single-crystal diamond substrate by now, which is electrically more advantageous than its polycrystalline counterpart, area yield and production cost highly disfavour the usage of scCVD diamonds in large-scale applications. Therefore research is underway to further improve the electrical and optical properties of pCVD diamonds, which are often characterised by quantities such as the charge collection distance (CCD).

The main goal of this thesis was to develop a transient current technique (TCT) setup which is applicable to various sensor materials, but especially in order to measure the CCD of diamond. The presented results show that the setup itself is verified using a well-known silicon diode. Characteristic quantities of the sample could be measured with high statistical accuracy. A more precise estimation of systematic uncertainties will be necessary in the near future to optimise the results regarding precision. In the end, the TCT setup could be used to measure a diamond sample and determine its CCD and thus the setup could fulfil that goal.

Regarding future developments, it would be better to include another operational amplifier on the board in order to achieve a higher gain on the signal and measure TCT signals in diamond more easily. In addition, there are many analyses which are not included in this thesis, either because of redundancy or since they are beyond the scope of this work.

In conclusion, the developed TCT setup works well with the presented samples.

Bibliography

[1] H. Bethe, *Zur Theorie des Durchgangs schneller Korpuskalarteilchen durch Materie* (in German), Ann. Phys. **5**, 325 (1930)

[2] F. Bloch, *Bremsvermögen von Atomen mit mehreren Elektronen* (in German), Z. Phys. **76**, 363 (1933)

[3] J. Beringer, et al. (Particle Data Group), *Review of Particle Physics*, Phys. Rev. D **86**, 010001 (2012)

[4] J. D. Jackson, *Classical Electrodynamics*, John Wiley & Sons, Inc., New York (1975)

[5] L. Landau, *On the energy loss of fast particles by ionization*, J. Phys. (USSR) **8**, 201 (1944)

[6] P. V. Vavilov, *Ionization losses of high-energy heavy particles*, Sov. Phys. JETP **5**, 749 (1957)

[7] H. Bichsel, *Straggling in Thin Silicon Detectors*, Rev. Mod. Phys. **60**, 663 (1988)

[8] Y.-S. Tsai, *Pair Production and Bremsstrahlung of Charged Leptons*, Rev. Mod. Phys. **46**, 815 (1974)

[9] L. Rossi, et al., *Pixel Detectors*, Springer Berlin Heidelberg (2006)

[10] G. Kramberger, *Signal development in irradiated silicon detectors*, Ph.D. thesis, University Ljubljana, Ljubljana (2001), *CERN-THESIS-2001-038*

[11] H. Pernegger, *High mobility diamonds and particle detectors*, phys. stat. sol. (a) **203(13)**, 3299 (2006)

[12] R. Wunstorf, *Systematische Untersuchungen zur Strahlenresistenz von Silizium-Detektoren für die Verwendung in Hochenergiephysik-Experimenten* (in German), Ph.D. thesis, Hamburg University, Hamburg (1992), *DESY-FH1K-92-01*

[13] M. Moll, *Radiation damage in silicon particle detectors: Microscopic defects and macroscopic properties*, Ph.D. thesis, Hamburg University, Hamburg (1999), *DESY-THESIS-1999-040*

[14] R. S. Balmer, et al., *Chemical vapour deposition synthetic diamond: materials, technology and applications*, J. Phys. Cond. Mat. **21**, 364221 (2009)

[15] R. P. Mildren, J. R. Rabeau, editors, *Optical Engineering of Diamond*, Wiley-VCH Verlag GmbH & Co. KGaA (2013)

[16] A. van der Drift, *Evolutionary selection, a principle governing growth orientation in vapour-deposited layers*, Philips Res. Rep. **22(3)**, 267 (1967)

[17] R. S. Sussmann, *Handbook of Ceramic Hard Materials*, WILEY-VCH Verlag, Weinheim (2000)

[18] D. Meier, *CVD Diamond Sensors for Particle Detection and Tracking*, Ph.D. thesis, Heidelberg University, Geneva (1999)

[19] A. Kok, et al., *Fabrication of 3D silicon sensors*, PoS **VERTEX 2010**, 022 (2010)

[20] H. O. Jeschke, et al., *Theory for laser-induced ultrafast phase transitions in carbon*, Appl. Phys. A **69(1)**, S49 (1999)

[21] H. O. Jeschke, et al., *Microscopic analysis of the laser-induced femtosecond graphitization of diamond*, Phys. Rev. B **60**, R3701 (1999)

[22] V. N. Strekalov, *Graphitization of diamond stimulated by electron-hole recombination*, Appl. Phys. A **80(5)**, 1061 (2005)

[23] V. N. Strekalov, et al., *Early stages of laser graphitization of diamond*, Appl. Phys. A **76(4)**, 603 (2003)

[24] T. V. Kononenko, et al., *Microstructuring of diamond bulk by IR femtosecond laser pulses*, Appl. Phys. A **90(4)**, 645 (2008)

[25] M. Neff, et al., *Femtosecond laser writing of buried graphitic structures in bulk diamond*, Appl. Phys. A **97(3)**, 543 (2009)

[26] H. C. Beck, *Charakterisierung von Graphitelektroden in Diamant* (in German), Bachelor's thesis, University Göttingen, Göttingen (2013), *II.Physik-UniGö-BSc-2013/07*

[27] A. Wadsworth (Agilent Technologies), *The Parametric Measurement Handbook*, 1st edition (2010)

[28] Agilent Technologies, *Agilent B1505A Power Device Analyzer/Curve Tracer - User's Guide*, 8th edition (2012)

[29] J. Becker, *Signal Development in Silicon Sensors Used for Radiation Detection*, Ph.D. thesis, Hamburg University, Hamburg (2010), *DESY-THESIS-10-033*

[30] F. Thuselt, *Physik der Halbleiterbauelemente* (in German), Springer Berlin Heidelberg, 2nd edition (2011)

[31] S. Ramo, *Currents induced by electron motion*, Proc. Ire. **27**, 584 (1939)

[32] J. H. Jeans, *The Mathematical Theory of Electricity and Magnetism*, Cambridge University Press, 5th edition (1927)

[33] M. Pfaff, *Dynamic Efficiency Measurements for Irradiated ATLAS Pixel Single Chip Modules*, Master's thesis, University Göttingen, Göttingen (2011), *II.Physik-UniGö-Dipl-2011/05*

[34] R. B. Firestone, L. P. Ekström, *WWW Table of Radioactive Isotopes* (2004), database version 2.1, URL `http://ie.lbl.gov/toi/index.htm`

[35] Analog Devices, *AD8000* 1.5 GHz *Ultrahigh Speed Op Amp - Data Sheet* (2013)

[36] H. Pernegger, et al., *Charge-carrier properties in synthetic single-crystal diamond measured with the transient-current technique*, J. Appl. Phys. **97(7)**, 073704 (2005)

[37] Advanced Laser Diode Systems, *Picosecond Injection Laser (PiLas) - Owner's Manual* (2004)

[38] C. Canali, G. Majni, R. Minder, G. Ottaviani, *Electron and hole drift velocity measurements in silicon and their empirical relation to electric field and temperature*, Electron Devices, IEEE Transactions on **22(11)**, 1045 (1975)

[39] L. Graber, *Characterisation of highly irradiated polycrystalline diamond sensors for ionising radiation*, Master's thesis, University Göttingen, Göttingen (2011), *II.Physik-UniGö-MSc-2011/01*

[40] Kolter Electronic, *VV1000-LC3E linear preamplifier - Data Sheet* (2014)

Erklärung nach §18(8) der Prüfungsordnung für den Bachelor-Studiengang Physik und den Master-Studiengang Physik an der Universität Göttingen:

Hiermit erkläre ich, dass ich diese Abschlussarbeit selbständig verfasst habe, keine anderen als die angegebenen Quellen und Hilfsmittel benutzt habe und alle Stellen, die wörtlich oder sinngemäß aus veröffentlichten Schriften entnommen wurden, als solche kenntlich gemacht habe.
Darüberhinaus erkläre ich, dass diese Abschlussarbeit nicht, auch nicht auszugsweise, im Rahmen einer nichtbestandenen Prüfung an dieser oder einer anderen Hochschule eingereicht wurde.

Göttingen, den September 4, 2015

(Christoph Klein)